Rare-Earth Gallium Garnet ($RE_3Ga_5O_{12}$, RE= Eu, Gd, Dy, Er, and Yb) self-assembled nanostructure based battery type electrodes for efficient asymmetric supercapacitor applications.

Bagavathy Shunmughananthan,[a] Thangaraju Dheivasigamani [a*], Jesman Sthevan Kovil Pitchai,[b]

[a]*Nano-crystal Design and Application Lab (n-DAL), Department of Physics, PSG Institute of Technology and Applied Research, Coimbatore-641062, Tamil Nadu, India*

[b]*Solid State Ionics Lab, PG & Research Department of Physics, Thanthai Periyar Government Arts and Science College (Autonomous), (Affiliated to Bharathidasan University), Tiruchirappalli-620023, Tamil Nadu, India*

Corresponding author:

*Thangaraju Dheivasigamani (dthangaraju@gmail.com)

Abstract

The modern energy crisis has recently prompted researchers to seek alternatives. In this context, using electrochemical energy resources for energy conversion and storage drew considerable interest. Herein, a new attempt at implementing a series of semiconducting rare earth gallium garnets (REGGs; RE= Eu, Gd, Dy, Er, and Yb)/$RE_3Ga_5O_{12}$ is employed for energy storage application. Garnets, an active host for rare earth ions with significant physical and chemical features, are expected to be promising electrode materials for supercapacitors. REGGs are synthesized via the gel matrix method. The phase purity and morphology of synthesized garnets were confirmed using XRD, Raman, XPS, FESEM, and TEM analysis. All synthesized rare earth gallium garnets show a cubic structure and manifest coral reef-like structures with minor variations. The surface area of the material is calculated using BET analysis. The electrochemical performance of the material is evaluated with CV, GCD, and EIS analysis in 3M KOH. $Eu_3Ga_5O_{12}$ exhibits a notable specific capacity of 303 C g^{-1} (84.1 mA h g^{-1}) at 1 A g^{-1} compared to other rare earth gallium garnets with sustained cyclic stability of about 80.12 % even after 5000 cycles. The practical applicability of the synthesized $Eu_3Ga_5O_{12}$ material is investigated by analyzing its performance in asymmetric supercapacitor devices. The fabricated device exhibited a maximum energy and power density of 39.06 W h Kg^{-1} and 1125 W kg^{-1} at 1 A g^{-1}, respectively. The exquisite features of rare earth gallium garnets with extended electrochemical performance indicate their potential to be a promising electrode material for energy storage applications.

Keywords: Rare earth gallium garnets, supercapacitor, Asymmetric device, Battery type electrodes

1. Introduction

The enormous usage of natural energy resources ultimately leads to the search for new generation power systems. Alternative approaches for replacing conventional energy resources have sparked significant interest, creating new solutions for powering vehicles and other appliances.[1,2] Recent research has focussed on clean and biocompatible energy sources, such as solar, geothermal, biomass, tidal, and wind power generation. However, the above-mentioned renewable power sources have an intermittent issue that creates a significant barrier between production and utilization, notably the need for continuous supply. This necessitates advanced power storage and conversion technology to utilize renewably produced power effectively.[3,4] Thus, research has focused on advances in effective storage systems to meet the current power need. Consequently, energy storage devices such as lithium-ion batteries and conventional capacitors[5] have become inevitable for renewable power generation. However, batteries have limited power density, shorter lifecycles, and overheating difficulties. In contrast, conventional capacitors have a low energy density, which provokes the development of a viable storage technology to address this concern. [6,7]

Supercapacitors, the next-generation storage device, have been discovered to be the most promising contender to tackle the energy storage challenges. Supercapacitors are electrochemical capacitors with very high capacitance. A supercapacitor can swiftly release or absorb energy and be charged or drained completely, whereas batteries take hours to charge. Thus, supercapacitors with a vast temperature range of operation,[8] low cost, speedy charge-discharge rates, and sustainable cyclic life can be used stand-alone or in conjunction with other components to amplify the power of batteries. [9,10] The electrochemical reaction on the electrode material surfaces is the basis for energy storage in a supercapacitor. Charges can be retained on its surface via the accumulation/separation (EDLC) and faradaic reaction processes (pseudo capacitor) that involve a fast reversible faradaic reaction to increase the energy density

than observed in EDLC-type capacitors.[6,11] Supercapacitors are the potential candidates with wide applications in electric and hybrid vehicles, energy backup systems, implantable medical devices such as pacemakers, and portable electronic devices.[12–14] Carbon-based materials, conducting polymers, metal oxides, and TMDCs are the most often explored and used electrode materials**.**[15,16] By optimizing the electrode material and the electrolyte, supercapacitors' energy storage capacity can be enhanced. The preferred electrode material must have greater electroconductivity and a large active surface area to improve supercapacitor performance.[17]

New garnet exploration has been increasing recently due to its multifunctional applicability in the energy and environmental sectors. The optimal garnet structure with $A_3B_2C_3O_{12}$ denotes A-dodecahedral, B-octahedral, and C-tetrahedral sites. Each cation is located on the core of the deformed oxygen polyhedron, forming a cubic crystallographic structure.[18,19] By changing or substituting the A and B site elements, diverse garnet structures can be synthesized, which alters their physical characteristics while the crystal structure remains unchanged.[20] The garnet lattice can be occupied with a range of rare-earth and transition metal ions, and the numerous doping sites provide more tuning possibilities for local site modifications.[21]

Garnets are one of the most significant classes of active hosts for the trivalent rare earth (RE^{3+}) ions due to their exceptional features, which include good chemical and thermal stability, strong optical abilities, and high hardness.[22] Rare earth elements have yet to be studied in energy storage technologies despite their substantial usage in optoelectronics, displays, solid-state illumination, lasers, imaging, and sensors.[23,24] The attributes of trivalent RE^{3+} ions exhibiting peculiar 4f configurations and containing unpaired 4f electrons that do not participate in chemical bonding aid in energy storage. RE elements are typically assumed to be chemically passive, yet most of them (Ce, Nd, Er, Dy, Pr, and Tm) possess either

RE^{4+}/RE^{3+} or RE^{3+}/RE^{2+} redox couples. This implies that rare earth-associated electrochemical storage is thermodynamically feasible.[25] The implementation of RE-based elements as positive grid enhancers in alkaline batteries[26] and metal hydride batteries[27] was facilitated by the massive ionic radius and the complicated coordination of rare earth elements, inducing the electrode materials lattice to be greatly deformed. In recent decades, the most commonly investigated Lutetium Aluminium Garnets (LAG),[28] Yttrium Aluminium Garnets (YAG),[27] Yttrium Iron Garnets (YIG),[29] Terbium Aluminium Garnets (TAG)[30] find innumerable applications in plasma displays, lasers, solar cells, scintillators, bioimaging, and phosphors. Their overall performance shall be increased by replacing aluminium with gallium atoms, as these garnets possess large unit cell volumes and an extended refractive index.[22] The ionic radius of gallium (0.62Å) is closer to that of Al^{3+} (0.535Å).[31] The covalent bonding of Ga-O in garnets favors the occupancy of Ga in the tetrahedral site more than the octahedral site. The four stable states that make up the rare earth gallium oxide system are perovskite, monoclinic, orthorhombic, and garnet crystal structures, which rely on the ionic sizes of the REs.[32] Garnets are usually synthesized using traditional methods such as the Czocharlski method,[33] geothermal,[32] co-precipitation, glass crystallization, mechanical alloying, and self-combustion techniques.[29]

There are quite a few reports in the literature about rare earth garnets used in energy storage. Torabian et al. reported the electrosynthesis of Poly-ortho aminophenol/$Al_5Y_3O_{12}$ nanocomposite as an efficient supercapacitor. $Al_5Y_3O_{12}$ (YAG) was synthesized by the pulse electrochemical deposition method, claiming that YAG had improved the active sites of the composites for increased faradaic reactions. The specific capacitance of about 237 F g^{-1} with a capacitive retention rate of 83% after 3000 cycles was observed for the prepared composites.[34] Yan Ling Hu et al. fabricated a hybrid structure of GaN/Ga_2O_3 micro rods on carbon cloth as high-performing electrodes for supercapacitor applications. The GaN/Ga_2O_3

hybrid structure is responsible for the exceptional electrochemical performance of the prepared electrode due to the absorb/redox active sites on the surface of Ga_2O_3. These active sites on the surface further enable faster electron transport.[35]

With the available reports, rare earth gallium garnet-based materials have yet to be widely explored as a potential energy storage material for batteries and supercapacitors. Investigating this series of rare earth gallium garnets other than traditional metal oxides, etc., could improve advancements in energy storage applications. This work focuses on synthesizing rare earth gallium garnets $RE_3Ga_5O_{12}$ (RE: Eu, Gd, Dy, Er, Tm &Yb) using the gel matrix method. Various studies thoroughly examined the garnet's phase formation and optical and chemical composition. The electrochemical performance of synthesized rare earth garnets has been investigated in the OrigaFlex-OGF500 workstation and explored their scope for supercapacitors.

2. Experimental Section

2.1 Synthesis of materials

For the synthesis of REGG, all the reagents were used without any purification. Trichlorogallane of (98%) purity was purchased from Tokyo Chemicals. 2-Hydroxypropane-1,2,3-tricarboxylic acid and ethane-1,2-diol were from SISCO and Merck Life Science. Rare earth nitrates were synthesized from rare earth oxides.

An array of REGG (RE = Eu^{3+}, Gd^{3+}, Dy^{3+}, Er^{3+}, and Yb^{3+}) particles were synthesized using the gel matrix method. A Prepared solution (50 ml) of 0.5mmole of rare earth ($RE(No_3)_3$. $6H_20$ [RE = Eu^{3+}, Gd^{3+}, Dy^{3+}, Er^{3+} and Yb^{3+})) mixed 0.83mmole of trichlorogallane ($GaCl_3$) were stirred. Herein, 1.3mmole of 2-hydroxypropane-1,2,3-tricarboxylic acid ($C_6H_8O_7.H_20$) was added, and the clear solution was heated at 70ºC. The binder, ethane-1,2-diol ($C_2H_6O_2$), which stimulates the polymerization of the formed complex, was added in drops.[12,36,37]

The resultant product is thermally treated at 950ºC after the evaporation of liquid species. The synthesized powders were cooled and collected. [38,39]

2.2 Characterization

The phase formation and the purity of the prepared novel REGG particles were examined with Powder X-ray Diffraction ('X'PERT PANalytical-PXRD) with Cu Kα radiation of wavelength 1.54 Å with 2θ ranging from 10º to 90º. The vibrational and spectral analysis of the synthesized materials were studied using a Horiba Jobin Yuvon HR 800 Raman spectrometer. The elemental composition of REGG and their oxidation states were obtained using X–ray photoelectron spectroscopy (XPS) from Thermo Scientific K – Alpha Surface Analysis using an Al source. The surface topography of the synthesized garnets is studied via ZEISS Sigma Field Emission Scanning Electron Microscopy (FESEM) and JOEL JEM -2100 Plus Transmission Electron Microscope (TEM) analysis. The material's surface area and pore size are analyzed using Quanta chrome Nova Station A Brunauer–Emmett–Teller (BET) analysis. Various analyses examined the electrochemical characteristics of rare earth gallium garnets in the Origa Flex – OGF500 electrochemical workstation.

2.3 Electrochemical measurement

For a three-electrode configuration, the active material, Ag/AgCl, and Pt wire act as working, reference, and counter electrodes, respectively. The active material, PVDF, and activated carbon (85, 5, and 10%) were added as additives to a solvent NMP for preparing a homogenous slurry. The active material used for the study is the as-synthesized $RE_3Ga_5O_{12}$ (RE = Eu, Gd, Dy, Er, and Yb). The slurry prepared is for the active electrode and of about 2 mg is coated on the nickel foam and kept under heat treatment at 70 ºC for 12 hrs. A Whatman filter paper separated the positive electrode (rare earth gallium garnets) and the negative electrode (AC) to permit the conductive ions to pass through. The electrochemical performance

of the prepared $RE_3Ga_5O_{12}$ (RE = Eu, Gd, Dy, Er, and Yb) was examined using three and two–electrode configurations in a 3M KOH electrolyte.

3. Results and discussion

Incorporating gallium and rare earth ions in the garnet structure provokes semiconducting behavior and shows energy-storing behavior. The search for effective energy storage materials and the synthesis procedure are schematically illustrated in Figure 1. Initially, the rare earth gallium garnet (REGG: RE = Eu, Gd, Dy, Er, and Yb) is synthesized using the gel matrix method. The solvents and the precursors are mixed well with citric acid, and ethylene glycol is added for gel formation. The cost-effective gel matrix method is adopted to prepare garnets to ensure the proper formation of single-phase $RE_3Ga_5O_{12}$ without any unwanted mixed phases. Thermally treated powders were characterized using various analytical techniques and employed for the energy storage device. The formation and crystal structure of the pristine rare earth gallium garnets are examined using XRD.

The X–ray diffraction pattern of the novel $RE_3Ga_5O_{12}$ (RE = Eu, Gd, Dy, Er, and Yb) with 2θ ranging from 20º to 90º is shown in Figure 2(a & b). All the prepared high-crystalline materials of the $RE_3Ga_5O_{12}$ family exhibit distinct diffraction peaks and correlate well with the standard observation. The pristine $RE_3Ga_5O_{12}$ (RE= Eu, Gd, Dy, Er, and Yb) garnets are of cubic structure in the Ia3d space group, resembling the similarities of rare earth elements. The lattice parameters of each RE garnet structure will be equal, i.e., (a = b = c), as they index the cubic crystallographic structure. The planes corresponding to the characteristic diffraction reflections of $RE_3Ga_5O_{12}$ (RE = Eu, Gd, Dy, Er, and Yb) are indexed in Figure 2(a & b). The intense high peak for all $RE_3Ga_5O_{12}$ garnets is centered at 2θ = 32º with little deviation. The observed satellite peak in three samples, such as $RE_3Ga_5O_{12}$ garnets (RE = Eu, Gd, Dy), were

identified as a slight amount of Ga_2O_3 and the same has not appeared in other rare-earth based gallium oxides (Er and Yb).[40]

The intense diffraction peaks of $RE_3Ga_5O_{12}$ garnets (RE = Eu, Gd, Dy, Er, and Yb) are compared and depicted in Figure 3. The intense peak at the (420) plane of rare earth gallium garnets significantly shifts towards a higher diffraction angle. The shift may be due to the change in ionic radii of the RE^{3+} ions in gallium garnets. The peak shift tends to move towards the higher end for the decrease in ionic radii. $Yb_3Ga_5O_{12}$ exhibits a higher shift than other $RE_3Ga_5O_{12,}$ as Yb^{3+} ions possess a lower ionic radius.

In addition, the vibrational properties of the pristine samples were analyzed using the Raman spectrum to identify the chemical structure. REGG's Raman spectrum ranges from 100 to 1100 cm^{-1}, separated into two regions: a lower frequency zone (150 -600 cm^{-1}) and a higher frequency zone (600 – 1070 cm^{-1}), accords with the results of YGG depicted in Figure 4. Comparatively, the spectrum of YAG contains three regions, as the volume of a unit cell of the gallium is larger than aluminium, ensuring the heavier gallium atom. The garnet lattice's unit cell holds four formula units of 80 atoms, and a factor group theory discloses 25 Raman active modes, which may be categorized into three A_{1g}, E_g, and T_{2g} modes.

The inner stretching vibration of the Ga atoms that is tetrahedrally coordinated is accountable for the bands in the area of high frequencies (800-1100 cm^{-1}) of the REGG spectrum. Ga atoms, trivalent cations with octahedral and dodecahedral coordination, and their translational and rotations are involved in the lattice modes in the frequencies area (150 - 415 cm^{-1}). GaO_6 octahedra and GaO_4 tetrahedra bonded at the corners form a network making up the REGG garnet structure. The RE^{3+} ions are accommodated in the dodecahedral cavities created by these polyhedra stacked in chains via the three crystallographic orientations. As the vibrations of the various polyhedra are closely related to each other, it is also feasible to

interpret the Raman spectra of garnets using the modes of vibrations of the tetrahedral (GaO_4), dodecahedral (REO_8) and octahedral (GaO_6) units.

The symmetric stretching vibration of the GaO_4 tetrahedron, in conjunction with the rotational mode encompassing the entire tetrahedron, is accountable for the band found at 338 cm^{-1} for $Eu_3Ga_5O_{12}$ and a minor shift for $RE_3Ga_5O_{12}$ (RE = Gd, Dy, Er and Yb) towards higher frequency. The translation of REO_8 (RE = Gd, Dy) units substantially influences the lattice constants and the mass of RE^{3+} ions, resulting in the lowest energy Eg phonons of $Gd_3Ga_5O_{12}$ at 162 and 292 cm^{-1} of $Dy_3Ga_5O_{12}$. The bending of the octahedron and dodecahedron molecular modes leads to the T_{2g} modes at 180 and 272 cm^{-1}, corresponding to Yb and Dy gallium garnets. Lower frequency E_g and T_{2g} vibrational modes can potentially study RE^{3+} ion occupancy of the dodecahedron site. The lattice and polyhedral O-Ga-O bending modes are liable to bands below 380 cm^{-1}. From the REGG spectrum, the observed E_g mode at a frequency of 415 is 460 and 515 cm^{-1} of T2g mode due to symmetric bending vibrations of the GaO_4 and GaO_6 units. The band recorded at about 730 cm^{-1} of $Eu_3Ga_5O_{12}$ is primarily caused by the symmetric stretching mode of the GaO_4 tetrahedron, although there may be a weaker influence from the anti-symmetric stretching mode.[41–45] This significantly strong band for $RE_3Ga_5O_{12}$ (RE = Gd, Dy, Er, and Yb) tends to shift towards a higher frequency zone. Consequently, the frequency drops as the mass of the RE^{3+} ions increase in $RE_3Ga_5O_{12}$, and thus, the observed REGG Raman spectrum is in accordance with the literature. The optical analysis and the bandgap calculation of $RE_3Ga_5O_{12}$ using the Tauc plot are provided in supporting information.

XPS analysis was carried out to examine the oxidation state and the chemical composition of the elements integrated into the gel matrix-derived rare earth gallium garnet. The survey spectrum of rare earth gallium garnets is shown in S3. The individual XPS spectra of RE^{3+} ions (RE= Eu, Gd, Dy, Er, and Yb), Ga, and O of garnets are shown in Figure 5(a-o). The XPS spectrum of Eu^{3+}, depicted in Figure 5(a), exhibits a strong peak centered around

1135.3 eV attributed to Eu $3d_{5/2}$ and an intense peak at 1145. 2eV is deconvoluted into two peaks, affirming the presence of Eu in the trivalent oxidation state of $Eu_3Ga_5O_{12}$.[46] Spectra of Gd 4d (Figure 5(d)) disclose a characteristic peak at 142.5 eV and a shoulder peak around 148.9 eV corresponding to Gd $4d_{5/2}$ and Gd $4d_{3/2}$ that are in accordance with the reports. The core level splitting in the Gd 4d spectrum is induced by spin-orbit coupling and sturdy 4d-4f exchange and interactions. The major peak is deconvoluted into two Gaussian curves. The characteristic peak at 142.5 eV of Gd 4d spectra may be attributed to the high-spin factor $4d^9$ $4f^7$ of parallel spin coupling, and the peak around 148.9 eV is of low spin factor arising from the anti-parallel spin coupling. Another small intense peak is observed at 161.6 eV, which might be attributed to the satellite peak.[47,48] Two intense distinct peaks of Dy 3d spectra shown in Figure 5(g) at binding energy 1296.9 and 1335.1 eV corresponds to Dy $3d_{5/2}$ and Dy $3d_{3/2}$, also deconvoluted into two peaks by curve fitting.[49] The XPS spectrum of Er 4d shown in Figure 5(j) comprises a Gaussian peak centered around 170.52 eV, confirming that Er exists in the trivalent state and is deconvoluted into two peaks.[50] Figure 5(m) depicts the XPS spectrum of Yb 4d with an intense characteristic peak at 186.3 eV attributed to Yb $4d_{5/2}$. A small satellite peak is observed around 189.6 eV.[51]

The Ga 3d spectrum shows a peak with different binding energies of $RE_3Ga_5O_{12}$ depicted in Figure 5(b, e, h, k and n). The Ga $3d_{5/2}$ peaks recorded at 20.9 and 20.7 eV of $RE_3Ga_5O_{12}$ (RE = Eu, Gd, Dy, Er and Yb) attributed to Ga – O bonds where Ga exists in the trivalent oxidation state, i.e., Ga $^{3+}$. Binding energies of Ga 3d peak around 21.2 – 21.8 eV is accountable to gallium nitride, oxide, or hydroxide. The peak with BE located at 18. 8 eV corresponds to Ga – Ga bonding. A characteristic little hump at 27, 25.4, 25.9, 27.2 and 27.8 eV could attribute to RE - Ga – O bonding (RE = Eu, Gd, Dy, Er and Yb). Consequently, this peak grows periodically, intense with a shift for other rare earth gallium garnets. Distortion in binding energies of Ga-O peaks was observed when comparing all Rare-earth Gallium Garnets

materials, which reveals there is no periodic effect while introducing different ionic radii rare earth ions in the garnet structure. The deconvoluted peak at binding energy 23.5 eV, owing to the O 2s core level contribution and the shift in the peak, can be observed for different $RE_3Ga_5O_{12}$.[52–55] Figure 5(c, f, i, l, and o) depicts the O 1s spectrum of REGG, exhibiting a characteristic peak whose binding energies range from 530.9 – 533.1 eV, may correspond to metal oxides, metal carbonates, and metal hydroxides. The O1s peak at 530.9 eV is attributed to the presence of Ga in the highest oxidation state Ga^{3+} of Ga_2O_3. The peak at 531.9 eV rises due to surface oxygen vacancies, and another one at 533.1 eV might be ascribed to C-O bonds. This further indicates the presence of trace amounts in the synthesized nanomaterials.[56]

The surface morphology may also affect the performance of the synthesized material. Therefore, the structural characteristics of $RE_3Ga_5O_{12}$ (RE = Eu, Gd, Dy, Er, and Yb) are examined using FE-SEM. Figure 6 depicts the FE-SEM images of $Eu_3Ga_5O_{12}$ (a-c), $Gd_3Ga_5O_{12}$ (d-f), $Dy_3Ga_5O_{12}$ (g-i), $Er_3Ga_5O_{12}$ (j-l), and $Yb_3Ga_5O_{12}$ (m-o). The FE-SEM micrographs of $Eu_3Ga_5O_{12}$ depict that the particles are stacked together, forming a puzzle-like structure. Upon magnification, it is evident that particles with different shapes are interlinked, and the pattern exists throughout the sample area, exhibiting the sample's homogeneity. For $Gd_3Ga_5O_{12}$, the elongated particles are interconnected, with a little difference in the shape obtained by $Eu_3Ga_5O_{12}$. The FE-SEM micrograph of $Dy_3Ga_5O_{12}$ showed that the garnets' pattern collapsed and the particles agglomerated. The bubble-like nanoparticles are composed of numerous tiny nanoparticles. The smaller-sized bubbles occupy the gap between the larger ones, making the agglomeration denser. The distorted pattern begins to be retrieved, which is apparent from images of $Er_3Ga_5O_{12}$. The nanostructured particles are combined and lined up, forming a lengthy stack of particles. There are no different patterns observed, yet they are oriented similarly. The morphology of $Yb_3Ga_5O_{12}$ seems similar to that of $Eu_3Ga_5O_{12}$, but many nanostructured particles merged, forming a uniform pattern. The coral reef-like structure

combines numerous nanostructures exhibited throughout the synthesized rare earth gallium garnets. As all the rare earth gallium garnets exhibited similar morphology, $Eu_3Ga_5O_{12}$ is subjected to studying its precise growth and development using TEM. Figure 7(a-d) depicts the TEM images of as-synthesized $Eu_3Ga_5O_{12}$. The $Eu_3Ga_5O_{12}$ nanoparticles are continuous in distribution. The self-assembled nature of $Eu_3Ga_5O_{12}$ is retained and is consistent with the surface morphology analysis. The HRTEM (Figure 7(e-h)) images resemble the formation of non-uniform stacked layers of sheet-like nanostructures. The alignment and growth of nanoparticles are oriented in random directions. The $Eu_3Ga_5O_{12}$ exhibits the lattice spacing of about 0.285 Å and 0.307 Å, corresponding to (420) and (400) planes. The SAED pattern confirms the development of multiple-layer nanostructures.

The obtained REGG nanoparticles were subjected to electrochemical analysis to validate their performance towards supercapacitor application. The CV, GCD, and EIS analysis were performed in the Origa Flex – OGF500 workstation. The cyclic voltammetry analysis is performed for the prepared REGG (RE = Eu, Gd, Dy, Er and Yb) in a three-electrode system in 3M of KOH. The cyclic voltammograms of REGGs can be seen in Figure 8: $Eu_3Ga_5O_{12}$ (a), $Gd_3Ga_5O_{12}$ (b), $Dy_3Ga_5O_{12}$ (c), $Er_3Ga_5O_{12}$ (d), and $Yb_3Ga_5O_{12}$ (e) with the potential window range of 0–0.5 V.

The cyclic voltammetry of REGGs was performed at the scan rate ranging from 5 – 100 mV/s. The cyclic voltammograms exhibit well-defined oxidation and reduction peaks, indicating the occurrence of faradaic reactions throughout the process.[57] Capacitance was attributable to the electro-sorption and migration of K^+ and OH^- in the electrode and electrolyte interface, represented by the surface redox peaks. The homogeneity of the CV curves with discrete oxidation and reduction peaks indicates greater reversibility and shape sustainment even at higher scan rates. The shift of oxidation and reduction peaks towards positive and negative potential as the scan rate rises due to the resistive influence of the electrode,

polarization, and rapid ion movements. The current responsiveness of the CV curve improves with the rise in scan rate, revealing a rapid charge transfer of the electrodes. The peaks in redox potential unveil the linear relation with current and scan rate owing to the diffusion-controlled process during scanning. The increase in the surface area of the CV curve and the scan rate affect the specific capacitance of the material.[58,59]. The cyclic voltammograms of $RE_3Ga_5O_{12}$ exhibit battery-type behavior; it is essential to determine the specific capacity (C_s) of electrodes in terms of C g^{-1} and mA h g^{-1}, which can be computed using CV and GCD curves.

GCD analysis examines the specific capacity of the synthesized $RE_3Ga_5O_{12}$ (RE = Eu, Gd, Dy, Er, and Yb) electrode material. Figure 9 shows the GCD curves of $Eu_3Ga_5O_{12}$ (a), $Gd_3Ga_5O_{12}$ (b), $Dy_3Ga_5O_{12}$ (c), $Er_3Ga_5O_{12}$ (d), and $Yb_3Ga_5O_{12}$ (e) with the potential range of 0.0–0.5 V at different current densities ranging from 1 Ag^{-1} to 5 A g^{-1}. The GCD curves retain their shapes even at high current density, ascertaining the excellent reversible redox reactions among the electrolyte and electrode.[60,61] The GCD curves show that the $Eu_3Ga_5O_{12}$ electrode leads to a higher discharge time than other $RE_3Ga_5O_{12}$ electrodes (RE = Gd, Dy, Er, and Yb). The discharge time tends to drop linearly with a rise in current density. The specific capacity of the corresponding $Eu_3Ga_5O_{12}$, $Gd_3Ga_5O_{12}$, $Dy_3Ga_5O_{12}$, $Er_3Ga_5O_{12}$, and $Yb_3Ga_5O_{12}$ is found to be 303 C g^{-1} (84.1 mA h g^{-1}), 180 C g^{-1} (50 mA h g^{-1}), 256 C g^{-1} (71.1 mA h g^{-1}), 216 C g^{-1} (60 mA h g^{-1}) and 261 C g^{-1} (72.5 mA h g^{-1}). The current density and the specific capacity are negatively correlated. Polarisation, reduced diffusion of ions in the electrolyte at increased current density, internal resistance, and the partial insertion reaction at possible active sites lead to the fall of specific capacitance.[59,62–64] Smaller IR drops appeared at the emerging discharge curves, indicating the faster diffusion of ions.[65] Figure 10(a) compares the specific capacity of REGGs with various current densities. Table 1 compares the specific capacity obtained for $RE_3Ga_5O_{12}$ (RE = Eu, Gd, Dy, Er, and Yb) over various ranges in current density.

Specific Capacity from GCD,

$$C_s = \frac{I\,\Delta t}{m} \qquad (C.g^{-1}) \tag{1}$$

$$C_s = \frac{I\,\Delta t}{m \times 3.6} \qquad (mAh.g^{-1}) \tag{2}$$

Where I signifies the current (mA), v is the scan rate (mV s^{-1}), Δt signifies the discharge time (s), Δv denotes the potential window (V), and the mass of the working material (mg) is represented by 'm'.[66]

For better insights into the durability of the supercapacitor, cyclic stability analysis was carried out, and the well-performed $Eu_3Ga_5O_{12}$ electrode was subjected to investigation. Figure 10(b) shows the capacitive retention graph of $Eu_3Ga_5O_{12}$. At a constant current density of 5 Ag^{-1}, the cyclic stability of the $Eu_3Ga_5O_{12}$ electrode is about 80.12% over 5000 cycles. The first few cycles of the 5000 charge-discharge cycles are inserted in Figure 10(b) to attain better knowledge. These studies show that among the synthesized rare earth gallium garnets, $Eu_3Ga_5O_{12}$ is affirmed as an excellent active material for electrodes with superior specific capacity and stability.

Materials with lower resistance are preferred for the practical application of supercapacitors that provoke rapid transportation of electrons and ions, enhancing the rate capability. The charge transport properties and the dynamics of the electrode process are characterized using EIS analysis. The EIS analysis was executed with a frequency range of 100 kHz to 0.01 Hz in a 3M KOH electrolyte. The comparative Nyquist plot (Imaginary part (-Z) vs. Real part (Z)) of the impedance of $RE_3Ga_5O_{12}$ (RE = Eu, Gd, Dy, Er, and Yb) is depicted in Figure 11(a) with an inserted equivalent fitted circuit. The three components of the Nyquist plots are: (i) the intersection point of the X-axis at the higher frequency is attributed to the

internal resistance of the electrode (Rs); (ii) the semi-circle part at a higher frequency area is accountable to the charge-transfer resistance (R_{CT}) at the interface of the electrode and electrolyte and (iii) the slope of the line at low-frequency zone indicates the Warburg's impedance which is the dissipation of ions in the electrolyte and thereby denoting the typical capacitive behavior.[67–69] The obtained R_{CT} values of $Eu_3Ga_5O_{12}$, $Gd_3Ga_5O_{12}$, $Dy_3Ga_5O_{12}$, $Er_3Ga_5O_{12}$, and $Yb_3Ga_5O_{12}$ are 5.398 Ω, 6.880 Ω, 6.343 Ω, 6.538 Ω and 6.198Ω respectively. The equivalent circuit converted using the EIS spectrum aids in identifying the physical changes of the electrode materials and helps determine the ohmic drop and the cell resistance. The prepared $Eu_3Ga_5O_{12}$ electrode exhibits lower Rs and Rct values than other REGG (RE = Gd, Dy, Er, and Yb)-based electrodes, symbolizing their efficient charge-transfer properties and capacitive behavior confirming their suitability for supercapacitor devices. Specific capacity increases with a drop in resistance values with improved bias potential.[15,70] CV and GCD results of $Eu_3Ga_5O_{12}$ electrode material correlate with the above EIS results. The electrodes were analyzed to assess their efficacy in the delivery of charges. Figure 11(b) shows the bode plot of synthesized materials. The system's efficiency heavily relies on the relaxation time constants obtained by analyzing the impedance spectra at a phase angle of 45°, specifically at the characteristic frequency "f_0". The relaxation time constant τ_0 has been determined using the equation (3),

$$\tau_0 = \frac{1}{f_0} \tag{3}$$

In this context, the terms "Relaxation time (τ_0)" and "Relaxation frequency (f_0)" are being discussed. The analysis of Bode plots for $Eu_3Ga_5O_{12}$, $Gd_3Ga_5O_{12}$, $Dy_3Ga_5O_{12}$, $Er_3Ga_5O_{12}$ and $Yb_3Ga_5O_{12}$ has provided valuable insights into the efficient charge delivery and degradation potential. These findings hold great promise for driving significant advancements in energy storage.[71,72]

$Eu_3Ga_5O_{12}$ exhibited excellent electrochemical behavior compared to other $RE_3Ga_5O_{12}$ (RE = Gd, Dy, Er and Yb). Further, the size and surface area of the synthesized $Eu_3Ga_5O_{12}$ is analyzed using the N_2 adsorption-desorption isotherm and pore size distribution depicted in Figure 12. According to the IUPAC classification, the resultant BET isotherm exhibits a typical type IV hysteresis loop, indicating the mesoporous structure of the particles. The phenomenon of capillary condensation in type IV isotherms combines hysteresis.[73] The surface area and the pore diameter of $Eu_3Ga_5O_{12}$ obtained from BET analysis are 35.73 m^2/g and 2.240 nm, respectively. The BJH analysis graph (inset of Figure 12) shows the pore size distribution of about 2 to 14nm of $Eu_3Ga_5O_{12}$. Surface area is not the only parameter that affects the capacitive behavior of the material but has an influence in increasing the specific capacitance.[74] Table 2 compares the electrochemical performance of synthesized material with that of the existing literature.

An asymmetric supercapacitor (ASC) device is fabricated to examine the electrochemical potential of the well-performing, synthesized $Eu_3Ga_5O_{12}$ material for practical usage in energy storage devices. In a two-electrode system, their electrochemical performance was analyzed with $Eu_3Ga_5O_{12}$ as a positive electrode and activated carbon (AC) as the negative electrode in 3M KOH. A Whatman filter paper acts as a separator between the electrodes. The schematic illustration of the charge storage mechanism of an asymmetric supercapacitor (ASC) device is shown in Figure 13. The stability of the voltage window for the ASC device can be assessed by performing CV for both the positive and negative electrodes. Owing to the principle of charge balance, the ratio of the mass of the electrodes was balanced using the equation (4):

$$\frac{m_+}{m_-} = \frac{C_- \times \Delta v_-}{C_+ \times \Delta v_+} \quad (4)$$

411 Where the mass, specific capacity, and potential window of positive and negative electrodes
412 are represented by $m_{\pm}$, $C_{\pm}$ and $\Delta v_{\pm,}$ correspondingly.[75]

413 The comparative CV profile of active material ($Eu_3Ga_5O_{12}$) and activated carbon at a
414 scan rate of 20 mV/s is shown in Figure 14(a) of two electrode configurations. Figure 14(b)
415 exhibits the CV voltammograms of $Eu_3Ga_5O_{12}$ and an AC-based asymmetric device in 3M
416 KOH, with the potential range corresponding to 0 to 0.5V and -1.0 to 0 V. The range of the
417 potential window results from the sum of the potential ranges of both electrodes. The voltage
418 window range is fixed at 0 – 1.5V for different scan rates throughout the CV analysis. The
419 cyclic voltammograms with a pair of oxidation and reduction peaks infer the combined EDLC
420 and battery-like behavior. The shape of CV curves sustained even at increased scan rates,
421 exhibiting their reversibility and extended rate capability of the fabricated ASC device. [15,76].
422 The GCD curves of the REGG-based ASC are shown in Figure 14(c) with varying current
423 densities. GCD analysis aids in determining the specific capacity of the fabricated asymmetric
424 supercapacitor device. The current density varied from 1 Ag^{-1} to 5 $Ag^{-1,}$ and the homogeneity
425 of the shape of GCD curves was retained throughout the analysis. The appearance of a plateau
426 in the discharge curve suggests incorporating a redox-active nature.[77] The $Eu_3Ga_5O_{12}$||AC
427 asymmetric supercapacitor exhibits a specific capacity of about 125 C g^{-1} (34.72 mA h. g^{-1}) at
428 a current density of 1 Ag^{-1}. The maximum energy density and the power density of the ASC
429 device at a current density of 1 Ag^{-1} are about 39.06 W h Kg^{-1} and 1125 W Kg^{-1}, respectively.
430 A swage-lock type device is used for investigating the cyclic stability of the fabricated device
431 by eliminating the barriers, and the depletion of initial stability arises from the fast kinetics at
432 the electrode interface and the electrolyte.[59] $Eu_3Ga_5O_{12}$-based ASC device shows a cyclic
433 stability of about 60.45 % after 10,000 cycles, and the device exhibited extended coulombic
434 efficiency of about 91.76 % at 5 Ag^{-1} depicted in Figure 14(d). The prolonged cyclic stability
435 with extended energy and power density makes the supercapacitor device prompt for practical

application. Table 3 shows the electrochemical performance and the obtained parameters of the fabricated $Eu_3Ga_5O_{12}$||AC ASC device. The coulombic efficiency was calculated using [78]:

$$\eta = \frac{t_D}{t_C} \tag{5}$$

Where t_D and t_C represent the corresponding discharging and charging time. The energy density (E) and the power density (P) of the device can be calculated from:

$$E = \frac{C \times \Delta v^2}{7.2} \ (Wh\ Kg^{-1}) \tag{6}$$

$$P = \frac{3600 \times E}{\Delta t} \ (W\ Kg^{-1}) \tag{7}$$

Where Δt and Δv are the discharge time(s) and potential window (V), and C is the specific capacity (C g^{-1}).[79] Table 4 shows the electrochemical performance comparison of fabricated asymmetric devices with the reports.

Figure 15 depicts the XRD pattern of $Eu_3Ga_5O_{12}$ after the stability experiment. The obtained diffraction patterns of $Eu_3Ga_5O_{12}$ are in accordance with standard data. The intense peak at (111) planes corresponds to the nickel substrate. The surface morphology of fabricated $Eu_3Ga_5O_{12}$ on nickel foam after 10,000 charge-discharge cyclic experiments is shown in Figure 16. The SEM micrographs confirm the presence of $Eu_3Ga_5O_{12}$ on the nickel foam's surface, and the particles are bound to its surface. After the experiment, the SEM images of $Eu_3Ga_5O_{12}$ revealed the hexagonal, thin sheet-like structures than TEM analysis which are randomly piled together. As far as we are aware, single-phase stable rare earth gallium garnets have yet to be used as an electrode material for a supercapacitor. These findings open the door for further investigating rare earth gallium garnets in various applications.

4. Conclusion

In brief, a series of rare earth gallium garnets for supercapacitor application were synthesized using the gel matrix method. Various analysis, including XRD, FESEM, TEM, Raman, and XPS, was performed to examine the formation of particles and their properties. The morphological analysis confirmed that the synthesized rare earth gallium garnets exhibited similar coral reef structures. The surface area of the synthesized material is calculated using BET analysis. The performance and suitability of REGGs (RE = Eu^{3+}, Gd^{3+}, Dy^{3+}, Er^{3+}, and Yb^{3+}) for sustainable energy storage applications were investigated using CV, GCD, and EIS. $Eu_3Ga_5O_{12}$ exposes a superior specific capacity of about 303 C g^{-1} among other REGGs at a current density of 1 A g^{-1}. The semiconducting garnets display a cyclic stability of 80.12% over 5000 cycles. The asymmetric supercapacitor device was fabricated from the better performance obtained by $Eu_3Ga_5O_{12}$ compared to others. The fabricated ASC device using $Eu_3Ga_5O_{12}$ exhibited an enhanced energy density of 39.06 W h Kg^{-1} and a maximum power density of about 1125 W kg^{-1} at 1 A g^{-1}. The cyclic stability is about 60.45% after 10,000 cycles at 5 Ag^{-1}. Rare earth gallium garnets exhibit excellent electrochemical performance, confirming their potential as an electrode material for future energy conservation.

Declaration of competing interest

The authors declare that they have no conflict of interest and have no relevant financial or non-financial interests to disclose.

Acknowledgement

Author Bagavathy Shunmughananthan extends gratitude to PSG management for providing PSG iTech fulltime research scholarship.

Author Contributions

All the authors contributed to the study's conception and design. Materials preparation, data collection, and analysis were performed by Bagavathy Shunmughananthan, Jesman

Sthevan Kovil Pitchai, Thangaraju Dheivasigamani. All authors read and approved the final manuscript.

CRediT Authorship contribution statement

Bagavathy Shunmughananthan: Writing - original draft, Particle synthesis, Methodology, **Thangaraju Dheivasigamani:** Conceptualization, Visualization, Methodology, Supervision, Writing - review & editing, **Jesman Sthevan Kovil Pitchai**: Electrochemical analysis, Methodology, Writing - review & editing.

References

[1] C. Vijay Anil Dai, C. Srinivasu, K. Suresh, T. Niranjan Kumar, K.V.Murthy, Optical and Luminescence properties of Sm^{3+} (0.5%) doped $BaO-B_2O_3$ Glass, Int. J. Recent Sci. Res. 10 (2019) 30693–30695.

[2] G. Wang, L. Zhang, J. Zhang, A review of electrode materials for electrochemical supercapacitors, Chem. Soc. Rev. 41 (2012) 797–828.

[3] P. Chen, G. Shen, Y. Shi, H. Chen, C. Zhou, Preparation and Characterization of Flexible Asymmetric Supercapacitors Based on Transition-Metal-Oxide Nanowire/Single-Walled Carbon Nanotube Hybrid Thin-Film Electrodes, 4 (2010) 4403–4411.

[4] Y. Zhao, D. Sun, G. Xing, M. Wei, J. Yang, X. Wang, D. Wang, Engineering 3D hybrid electrode composed of ceria nanoparticles embedded in nickel oxides for high-performance supercapacitors, J. Appl. Phys. 126 (2019) 015103.

[5] S. Vedi, T. Dheivasigamani, G.S. Selvam, T. Kawakami, N. Rajeswaran, S. Rajendran, A. Muthukaruppan, S. AlFaify, M. Shkir, Growth optimization of single-phase novel colloidal perovskite $Cs_3Bi_2I_9$ nanocrystals and $Cs_3Bi_2I_9$@SiO_2 core-shell nanocomposites for bio-medical application, Biomater. Sci. 10 (2022) 5956–5967.

[6] N. Joseph, P.M. Shafi, A.C. Bose, Recent Advances in 2D-$MoS_2$and its Composite Nanostructures for Supercapacitor Electrode Application, Energy and Fuels. 34 (2020) 6558–6597.

[7] Q. Meng, K. Cai, Y. Chen, L. Chen, Research progress on conducting polymer based supercapacitor electrode materials, Nano Energy. 36 (2017) 268–285.

[8] W. Zhang, Z. Shahnavaz, X. Yan, X. Huang, S. Wu, H. Chen, J. Pan, T. Li, J. Wang, One-Step Solvothermal Synthesis of Raspberry-like NiCo-MOF for High-Performance Flexible Supercapacitors for a Wide Operation Temperature Range, Inorg. Chem. 61 (2022) 15287–15301.

[9] M. Sharma, A. Gaur, Cu Doped Zinc Cobalt Oxide Based Solid-State Symmetric Supercapacitors: A Promising Key for High Energy Density, J. Phys. Chem. C. 124 (2020) 9–16.

[10] S. Xu, X. Li, Z. Yang, T. Wang, W. Jiang, C. Yang, S. Wang, N. Hu, H. Wei, Y. Zhang, Nanofoaming to Boost the Electrochemical Performance of Ni@$Ni(OH)_2$ Nanowires for Ultrahigh Volumetric Supercapacitors, ACS Appl. Mater. Interfaces. 8 (2016) 27868–27876.

[11] S. Arunachalam, B. Kirubasankar, D. Pan, H. Liu, C. Yan, Z. Guo, S. Angaiah, Research progress in rare earths and their composites based electrode materials for supercapacitors, Green Energy Environ. 5 (2020) 259–273.

[12] D. Thangaraju, S. Moorthy Babu, P. Samuel, A. Durairajan, Y. Hayakawa, Influence of pH and microwave calcination on the morphology of $KGd(WO_4)_2$ particles derived by Pechini Sol-Gel method, J. Sol-Gel Sci. Technol. 58 (2011) 419–426.

[13] S. Sundriyal, V. Shrivastav, H. Kaur, S. Mishra, A. Deep, High-Performance Symmetrical Supercapacitor with a Combination of a ZIF-67/rGO Composite Electrode and a Redox Additive Electrolyte, ACS Omega. 3 (2018) 17348–17358.

[14] J. Yan, Q. Wang, T. Wei, Z. Fan, Recent advances in design and fabrication of electrochemical supercapacitors with high energy densities, Adv. Energy Mater. 4 (2014) 1300816.

[15] B. Shunmughananthan, T. Dheivasigamani, J. Sthevan Kovil Pitchai, S. Periyasamy, Performance comparison of distinct bismuth molybdate single phases for asymmetric supercapacitor applications, Dalt. Trans. 51 (2022) 15579–15592.

[16] G.S. Selvam, T. Dheivasigamani, A. Prabhu, N.K. Mani, Embellishing 2-D MoS_2Nanosheets on Lotus Thread Devices for Enhanced Hydrophobicity and Antimicrobial Activity, ACS Omega. 7 (2022) 24606–24613.

[17] E.H. Lahrar, P. Simon, C. Merlet, Carbon-carbon supercapacitors: Beyond the average pore size or how electrolyte confinement and inaccessible pores affect the capacitance, J. Chem. Phys. 155 (2021) 184703.

[18] Y. Yang, T. Liu, L. Bi, L. Deng, Recent advances in development of magnetic garnet thin films for applications in spintronics and photonics, J. Alloys Compd. 860 (2021) 158235.

[19] Y.P. Vorob'ev, O. V. Karban, Defect structure of rare-earth gallium germanium garnets, Inorg. Mater. 36 (2000) 718–725.

549 [20] S. Abouali, C.H. Yim, A. Merati, Y. Abu-Lebdeh, V. Thangadurai, Garnet-Based
550 Solid-State Li Batteries: From Materials Design to Battery Architecture, ACS Energy
551 Lett. 6 (2021) 1920–1941.

552 [21] S. Wang, J. Zhang, G. Jing, Z. Ye, H. Yu, H. Zhang, Exploring impurity phases
553 derived from the introduction of vanadium ions in yttrium gallium garnet, Ceram. Int.
554 46 (2020) 25996–26003.

555 [22] V. Monteseguro, M. Rathaiah, K. Linganna, A.D. Lozano-Gorrín, M.A. Hernández-
556 Rodríguez, I.R. Martín, P. Babu, U.R. Rodríguez-Mendoza, F.J. Manjón, A. Muñoz,
557 C.K. Jayasankar, V. Venkatramu, V. Lavín, Chemical pressure effects on the
558 spectroscopic properties of Nd^{3+} doped gallium nano-garnets, Opt. Mater. Express. 5
559 (2015) 1661.

560 [23] W. Gao, D. Wen, J.C. Ho, Y. Qu, Incorporation of rare earth elements with transition
561 metal–based materials for electrocatalysis: a review for recent progress, Mater. Today
562 Chem. 12 (2019) 266–281.

563 [24] H. Zhao, J. Xia, D. Yin, M. Luo, C. Yan, Y. Du, Rare earth incorporated electrode
564 materials for advanced energy storage, Coord. Chem. Rev. 390 (2019) 32–49.

565 [25] S. Liang, H. Wang, Y. Li, H. Qin, Z. Luo, B. Huang, X. Zhao, C. Zhao, L. Chen, Rare-
566 earth based nanomaterials and their composites as electrode materials for high
567 performance supercapacitors: A review, Sustain. Energy Fuels. 4 (2020) 3825–3847.

568 [26] W. Zhang, A. Li, H. Chen, B. Lan, K. Pan, T. Zhang, M. Fang, S. Liu, W. Zhang, The
569 effect of rare earth metals on the microstructure and electrochemical corrosion
570 behavior of lead calcium grid alloys in sulfuric acid solution, J. Power Sources. 203
571 (2012) 145–152.

[27] J.C.A. Santos, E.P. Silva, D. V. Sampaio, D.C. Silva, N.R.S. Souza, C. Kucera, J. Ballato, R.S. Silva, Effect of the Ce^{3+} concentration on laser-sintered YAG ceramics for white LEDs applications, J. Eur. Ceram. Soc. 40 (2020) 3673–3678.

[28] Y. Liu, Y. Cao, L. Huang, M. Gao, H. Pan, Rare earth-Mg-Ni-based hydrogen storage alloys as negative electrode materials for Ni/MH batteries, J. Alloys Compd. 509 (2011) 675–686.

[29] M. Niaz Akhtar, M. Azhar Khan, M. Ahmad, G. Murtaza, R. Raza, S.F. Shaukat, M.H. Asif, N. Nasir, G. Abbas, M.S. Nazir, M.R. Raza, $Y_3Fe_5O_{12}$ nanoparticulate garnet ferrites: Comprehensive study on the synthesis and characterization fabricated by various routes, J. Magn. Magn. Mater. 368 (2014) 393–400.

[30] M. Geho, T. Sekijima, T. Fujii, Growth mechanism of incongruently melting terbium aluminum garnet ($Tb_3Al_5O_{12}$; TAG) single crystals by laser FZ method, J. Cryst. Growth. 275 (2005) 663–667.

[31] I.I. Vrubel, R.G. Polozkov, I.A. Shelykh, V.M. Khanin, P.A. Rodnyi, C.R. Ronda, Bandgap Engineering in Yttrium-Aluminum Garnet with Ga Doping, Cryst. Growth Des. 17 (2017) 1863–1869.

[32] M. Inoue, T. Nishikawa, H. Otsu, H. Kominami, T. Inui, Synthesis of rare-earth gallium garnets by the glycothermal method, J. Am. Ceram. Soc. 81 (1998) 1173–1183.

[33] M.A. Digiuseppe, Rare Earth Gallium Garnet Crystal Growth and Related Chemistry, Solid State Chem. 14 (1980) 277–290.

[34] J. Torabian, M.G. Mahjani, H. Mohammad Shiri, A. Ehsani, J. Shabani Shayeh, Facile electrosynthesis, characterisation and electrochemical performance of poly: Ortho

595 aminophenol/$Al_5Y_3O_{12}$ nanocomposite as a new high efficient supercapacitor, RSC
596 Adv. 6 (2016) 41045–41052.

597 [35] Y.L. Hu, Z. Wang, R. Yuan, Z. Xu, Y. Dai, B. Wang, Y. Fu, M. Ye, Y. Yang, Z. Zou,
598 C. Jiang, A hybrid GaN/Ga_2O_3 structure anchored on carbon cloth as a high-
599 performance electrode of supercapacitors, Dalt. Trans. 7 (2022).

600 [36] D. Thangaraju, A. Durairajan, D. Balaji, S. Moorthy Babu, Y. Hayakawa, SiO
601 2/$KGd(WO_4)_2$:Eu^{3+} composite luminescent nanoparticles: Synthesis and
602 characterization, Mater. Chem. Phys. 135 (2012) 1115–1121.

603 [37] P. Shanmugam, T. Dheivasigamani, S. Moorthy Babu, M. Shkir, E. El Sayed
604 Massoud, R. Marnadu, V.R. Minnam Reddy, A facile sol–gel synthesis and
605 characterization of europium (Eu) doped β-$Bi_2Mo_2O_9$ nanoparticles with remarkably
606 enhanced photocatalytic activity for waste-water treatments, Inorg. Chem. Commun.
607 146 (2022) 110163.

608 [38] A. Durairajan, D. Thangaraju, D. Balaji, S. Moorthy Babu, Sol-gel synthesis and
609 characterizations of crystalline $NaGd(WO_4)_2$ powder for anisotropic transparent
610 ceramic laser application, Opt. Mater. (Amst). 35 (2013) 740–743.

611 [39] D. Thangaraju, A. Durairajan, D. Balaji, S. Moorthy Babu, Synthesis and
612 characterization of monoclinic $KGd(WO_4)_2$ particles for non-cubic transparent
613 ceramics, Opt. Mater. (Amst). 35 (2013) 753–756.

614 [40] S. Kumar, G. Sarau, C. Tessarek, M.Y. Bashouti, A. Hähnel, S. Christiansen, R. Singh,
615 Study of iron-catalysed growth of β-Ga_2O_3 nanowires and their detailed
616 characterization using TEM, Raman and cathodoluminescence techniques, J. Phys. D.
617 Appl. Phys. 47 (2014).

[41] J.-J. Song, P.B. Klein, R.L. Wadsack, M. Selders, S. Mroczkowski, R.K. Chang, Raman-active phonons in aluminum, gallium, and iron garnets, J. Opt. Soc. Am. 63 (1973) 1135.

[42] E. Cavalli, E. Zannoni, M. Bettinelli, A. Speghini, M. Tonelli, A. Toncelli, Vibrational properties of $Ca_3Sc_2Ge_3O_{12}$, a garnet host crystal for laser applications, J. Phys. Condens. Matter. 12 (2000) 4665–4674.

[43] V. Monteseguro, P. Rodríguez-Hernández, H.M. Ortiz, V. Venkatramu, F.J. Manjón, C.K. Jayasankar, V. Lavín, A. Muñoz, Structural, elastic and vibrational properties of nanocrystalline lutetium gallium garnet under high pressure, Phys. Chem. Chem. Phys. 17 (2015) 9454–9464.

[44] V. Venkatramu, S.F. León-Luis, U.R. Rodríguez-Mendoza, V. Monteseguro, F.J. Manjón, A.D. Lozano-Gorrín, R. Valiente, D. Navarro-Urrios, C.K. Jayasankar, A. Muñoz, V. Lavín, Synthesis, structure and luminescence of Er^{3+} doped $Y_3Ga_5O_{12}$ nano-garnets, J. Mater. Chem. 22 (2012) 13788–13799.

[45] V. Venkatramu, M. Giarola, G. Mariotto, S. Enzo, S. Polizzi, C.K. Jayasankar, F. Piccinelli, M. Bettinelli, A. Speghini, Nanocrystalline lanthanide-doped $Lu_3Ga_5O_{12}$ garnets: Interesting materials for light-emitting devices, Nanotechnology. 21 (2010) 175703.

[46] X. Gong, H. Jiang, M. Cao, Z. Rao, X. Zhao, A. Vomiero, Eu-doped ZnO quantum dots with solid-state fluorescence and dual emission for high-performance luminescent solar concentrators, Mater. Chem. Front. 5 (2021) 4746–4755.

[47] N. Ullah, M. Imran, K. Liang, C.Z. Yuan, A. Zeb, N. Jiang, U.Y. Qazi, S. Sahar, A.W. Xu, Highly dispersed ultra-small Pd nanoparticles on gadolinium hydroxide nanorods for efficient hydrogenation reactions, Nanoscale. 9 (2017) 13800–13807.

[48] E. Talik, J. Kisielewski, P. Zajdel, A. Guzik, E. Wierzbicka, A. Kania, J. Kusz, S. Miga, M. Szubka, XPS spectroscopy, structural, magnetic and dielectric investigations of $CaGdAlO_4$ and Yb:$CaGdAlO_4$ single crystals, Opt. Mater. (Amst). 91 (2019) 355–362.

[49] B.G. Zhai, M.M. Chen, Y.M. Huang, Photoluminescence and afterglow of Dy^{3+} doped $CaAl_2O_4$ derived via sol-gel combustion, RSC Adv. 12 (2022) 31757–31768.

[50] H. Wen, J. He, J. Hong, S. Jin, Z. Xu, H. Zhu, J. Liu, G. Sha, F. Yue, Y. Dan, Efficient Er/O-Doped Silicon Light-Emitting Diodes at Communication Wavelength by Deep Cooling, Adv. Opt. Mater. 8 (2020) 2000720.

[51] E.R. López-Mena, O. Ceballos-Sanchez, T.J.N. Hooper, G. Sanchez-Ante, M. Rodríguez-Muñoz, J.A. Renteria-Salcedo, A. Elías-Zuñiga, A. Sanchez-Martinez, The effect of Yb doping on ZnO thin films obtained via a low-temperature spin coating method, J. Mater. Sci. Mater. Electron. 32 (2021) 347–359.

[52] A. Petitmangin, B. Gallas, C. Hebert, J. Perrière, L. Binet, P. Barboux, X. Portier, Characterization of oxygen deficient gallium oxide films grown by PLD, Appl. Surf. Sci. 278 (2013) 153–157.

[53] D. Li, M. Sumiya, S. Fuke, D. Yang, D. Que, Y. Suzuki, Y. Fukuda, Selective etching of GaN polar surface in potassium hydroxide solution studied by x-ray photoelectron spectroscopy, J. Appl. Phys. 90 (2001) 4219–4223.

[54] E.J. Rubio, T.E. Mates, S. Manandhar, M. Nandasiri, V. Shutthanandan, C. V. Ramana, Tungsten incorporation into gallium oxide: Crystal structure, surface and interface chemistry, thermal stability, and interdiffusion, J. Phys. Chem. C. 120 (2016) 26720–26735.

[55] J. Wu, Ye and Yang, Jiquan and Lin, Yingcheng and Xu, Synthesis of Samarium-Based Metal Organic Compound Nanoparticles with, Molecules. 24 (2019) 3657.

[56] A.K. Mondal, R. Deivasigamani, L.K. Ping, M.A. Shazni Mohammad Haniff, B.T. Goh, R.H. Horng, M.A. Mohamed, Heteroepitaxial Growth of an Ultrathin β-Ga_2O_3 Film on a Sapphire Substrate Using Mist CVD with Fluid Flow Modeling, ACS Omega. 7 (2022) 41236–41245.

[57] A.A. Mirghni, K.O. Oyedotun, O. Olaniyan, B.A. Mahmoud, N.F. Sylla, N. Manyala, Electrochemical analysis of Na-Ni bimetallic phosphate electrodes for supercapacitor applications, RSC Adv. 9 (2019) 25012–25021.

[58] G.P. Kamble, A.A. Kashale, A.S. Rasal, S.A. Mane, R.A. Chavan, J.Y. Chang, Y.C. Ling, S.S. Kolekar, A. V. Ghule, Marigold micro-flower like $NiCo_2O_4$ grown on flexible stainless-steel mesh as an electrode for supercapacitors, RSC Adv. 11 (2021) 3666–3672.

[59] J. Sthevan Kovil Pitchai, T. Dheivasigamani, B. Shunmughananthan, R. Arunagiri, S. Periyasamy, Single-wall and graphene-modified multiwall wasp nest shaped $Bi_2Mo_2O_9$ self-assembly for performance-enhanced asymmetric supercapacitor, J. Mater. Chem. C. 10 (2022) 16453–16464.

[60] S. Nongthombam, N.A. Devi, S. Sinha, R. Bhujel, S. Rai, W. Ishwarchand, S. Laha, B.P. Swain, Reduced graphene oxide/gallium nitride nanocomposites for supercapacitor applications, J. Phys. Chem. Solids. 141 (2020) 109406.

[61] S. Wu, F. Xue, M. Wang, J. Wang, Construction and electrochemical performances of the three-dimensional nano $NiCo_2O_4$, Integr. Ferroelectr. 189 (2018) 158–164.

[62] M. Isacfranklin, R. Yuvakkumar, G. Ravi, S.I. Hong, F. Shini, M. Thambidurai, C.

Dang, D. Velauthapillai, Marigold flower like structured Cu_2NiSnS_4 electrode for high energy asymmetric solid state supercapacitors, Sci. Rep. 10 (2020) 19198.

[63] Y. Feng, W. Liu, Y. Wang, W. Gao, J. Li, K. Liu, X. Wang, J. Jiang, Oxygen vacancies enhance supercapacitive performance of $CuCo_2O_4$ in high-energy-density asymmetric supercapacitors, J. Power Sources. 458 (2020) 228005.

[64] W. Ma, H. Nan, Z. Gu, B. Geng, X. Zhang, Superior performance asymmetric supercapacitors based on $ZnCo_2O_4$@MnO_2 core-shell electrode, J. Mater. Chem. A. 3 (2015) 5442–5448.

[65] M. Fahim, A. ul H.A. Shah, S. Bilal, Highly stable and efficient performance of binder-free symmetric supercapacitor fabricated with electroactive polymer synthesized via interfacial polymerization, Materials. 12 (2019) 1626.

[66] M. Isacfranklin, R. Yuvakkumar, G. Ravi, D. Velauthapillai, Morphological evolution of carnation flower-like Cu_2CoSnS_4 battery-type electrodes, Mater. Adv. (2022) 6643–6655.

[67] J. Sun, X. Du, R. Wu, Y. Zhang, C. Xu, H. Chen, Bundlelike $CuCo_2O_4$ Microstructures Assembled with Ultrathin Nanosheets As Battery-Type Electrode Materials for High-Performance Hybrid Supercapacitors, ACS Appl. Energy Mater. 3 (2020) 8026–8037.

[68] C. Liu, W. Jiang, F. Hu, X. Wu, D. Xue, Mesoporous $NiCo_2O_4$ nanoneedle arrays as supercapacitor electrode materials with excellent cycling stabilities, Inorg. Chem. Front. 5 (2018) 835–843.

[69] C. Wang, H. Tian, J. Jiang, T. Zhou, Q. Zeng, X. He, P. Huang, Y. Yao, Facile Synthesis of Different Morphologies of Cu_2SnS_3 for High-Performance

Supercapacitors, ACS Appl. Mater. Interfaces. 9 (2017) 26038–26044.

[70] Y. Shao, M.F. El-Kady, J. Sun, Y. Li, Q. Zhang, M. Zhu, H. Wang, B. Dunn, R.B. Kaner, Design and Mechanisms of Asymmetric Supercapacitors, Chem. Rev. 118 (2018) 9233–9280.

[71] S. Zhang, L. Sui, H. Dong, W. He, L. Dong, L. Yu, High-Performance Supercapacitor of Graphene Quantum Dots with Uniform Sizes, ACS Appl. Mater. Interfaces. 10 (2018) 12983–12991.

[72] T.A. Raja, P. Vickraman, A.S. Justin, B.J. Reddy, Ultrasonicated graphene quantum dots dispersoid zinc ammonium phosphate hybrid electrode for supercapacitor applications, J. Mater. Sci. Mater. Electron. 33 (2022) 7079–7098.

[73] Aashima, S. Uppal, A. Arora, S. Gautam, S. Singh, R.J. Choudhary, S.K. Mehta, Magnetically retrievable Ce-doped Fe3O4 nanoparticles as scaffolds for the removal of azo dyes, RSC Adv. 9 (2019) 23129–23141.

[74] B. Gnana Sundara Raj, A.M. Asiri, A.H. Qusti, J.J. Wu, S. Anandan, Sonochemically synthesized MnO_2 nanoparticles as electrode material for supercapacitors, Ultrason. Sonochem. 21 (2014) 1933–1938.

[75] S. Sanati, R. Abazari, A. Morsali, A.M. Kirillov, P.C. Junk, J. Wang, An Asymmetric Supercapacitor Based on a Non-Calcined 3D Pillared Cobalt(II) Metal-Organic Framework with Long Cyclic Stability, Inorg. Chem. 58 (2019) 16100–16111.

[76] S. Ghosh, P. Samanta, P. Samanta, N.C. Murmu, T. Kuila, Investigation of Electrochemical Charge Storage Efficiency of $NiCo_2Se_4$/RGO Composites Derived at Varied Duration and Its Asymmetric Supercapacitor Device, Energy and Fuels. 34 (2020) 13056–13066.

[77] L. Halder, A. Maitra, A.K. Das, R. Bera, S.K. Karan, S. Paria, A. Bera, S.K. Si, B.B. Khatua, Fabrication of an Advanced Asymmetric Supercapacitor Based on Three-Dimensional Copper-Nickel-Cerium-Cobalt Quaternary Oxide and GNP for Energy Storage Application, ACS Appl. Electron. Mater. 1 (2019) 189–197.

[78] J. Jiang, Z. Li, X. He, Y. Hu, F. Li, P. Huang, C. Wang, Novel Skutterudite CoP_3–Based Asymmetric Supercapacitor with Super High Energy Density, Small. 16 (2020) 2000180.

[79] S. Asaithambi, P. Sakthivel, M. Karuppaiah, R. Yuvakkumar, K. Balamurugan, T. Ahamad, M.A.M. Khan, G. Ramalingam, M.K.A. Mohammed, G. Ravi, Preparation of Fe-SnO_2@CeO_2 nanocomposite electrode for asymmetric supercapacitor device performance analysis, J. Energy Storage. 36 (2021) 102402.

[80] A. Nashim, S. Pany, K.M. Parida, Systematic investigation on the charge storage behavior of $GdCrO_3$ in aqueous electrolyte, J. Energy Storage. 42 (2021) 103145.

[81] M.P. Harikrishnan, A.J.C. Mary, A.C. Bose, Electrochemical performance of $ANiO_3$ (A= La, Ce) perovskite oxide material and its device performance for supercapattery application, Electrochim. Acta. 362 (2020) 137095.

[82] A.S. Keshari, P. Dubey, Sucrose-assisted one step hydrothermal synthesis of $MnCO_3$/Mn_3O_4 hybrid materials for electrochemical energy storage, Electrochim. Acta. 402 (2022) 139486.

[83] Y.A. Kumar, H.T. Das, P.R. Guddeti, R.R. Nallapureddy, M.R. Pallavolu, S. Alzahmi, I.M. Obaidat, Self-Supported Co_3O_4 @ Mo-Co_3O_4 Needle-like Nanosheet Heterostructured Architectures of Battery-Type Electrodes for High-Performance Asymmetric Supercapacitors, Nanomaterials. 12 (2022) 2330.

[84] P. Shanmugam, T. Dheivasigamani, J.S. Kovil Pitchai, A. Muthukaruppan, Stable single phases of samarium gallium oxide ($Sm_3Ga_xO_y$) nano semiconductor self-assembly for supercapacitor and photocatalytic applications, Dalt. Trans. 52 (2023) 5366–5382.

[85] S. Asaithambi, V. Balaji, M. Karuppaiah, P. Sakthivel, K. Muhil Eswari, R. Yuvakkumar, P. Selvakumar, D. Velauthapillai, G. Ravi, The electrochemical energy storage and photocatalytic performances analysis of rare earth metal (Tb and Y) doped SnO_2@CuS composites, Adv. Powder Technol. 33 (2022) 103442.

[86] S. Ahmad, K. Jabbour, M. Rafeeq, A. Naz, K.F. Fawy, S. Manzoor, M. Abdullah, N. Ghazouani, A. Mir, M.N. Ashiq, Effect on physiochemical assets of Dy added spinel $ZnSm_2O_4$ for energy storage applications, Ceram. Int. 49 (2023) 28036–28047.

[87] A. Kumar, A. Kumar, A. Kumar, Energy storage properties of double perovskites Gd_2NiMnO_6 for electrochemical supercapacitor application, Solid State Sci. 105 (2020) 106252.

[88] M.A. Kamran, W. Ali, S. Ullah, T. Alharbi, Q. Gul, Facile preparation of Ga-doped ZnO nanostructures by composite-hydroxide-mediated synthesis route for high-performance pseudocapacitors, J. Energy Storage. 62 (2023) 106871.

779

780

781

782

783

784

785

786

787

788

789

790

791

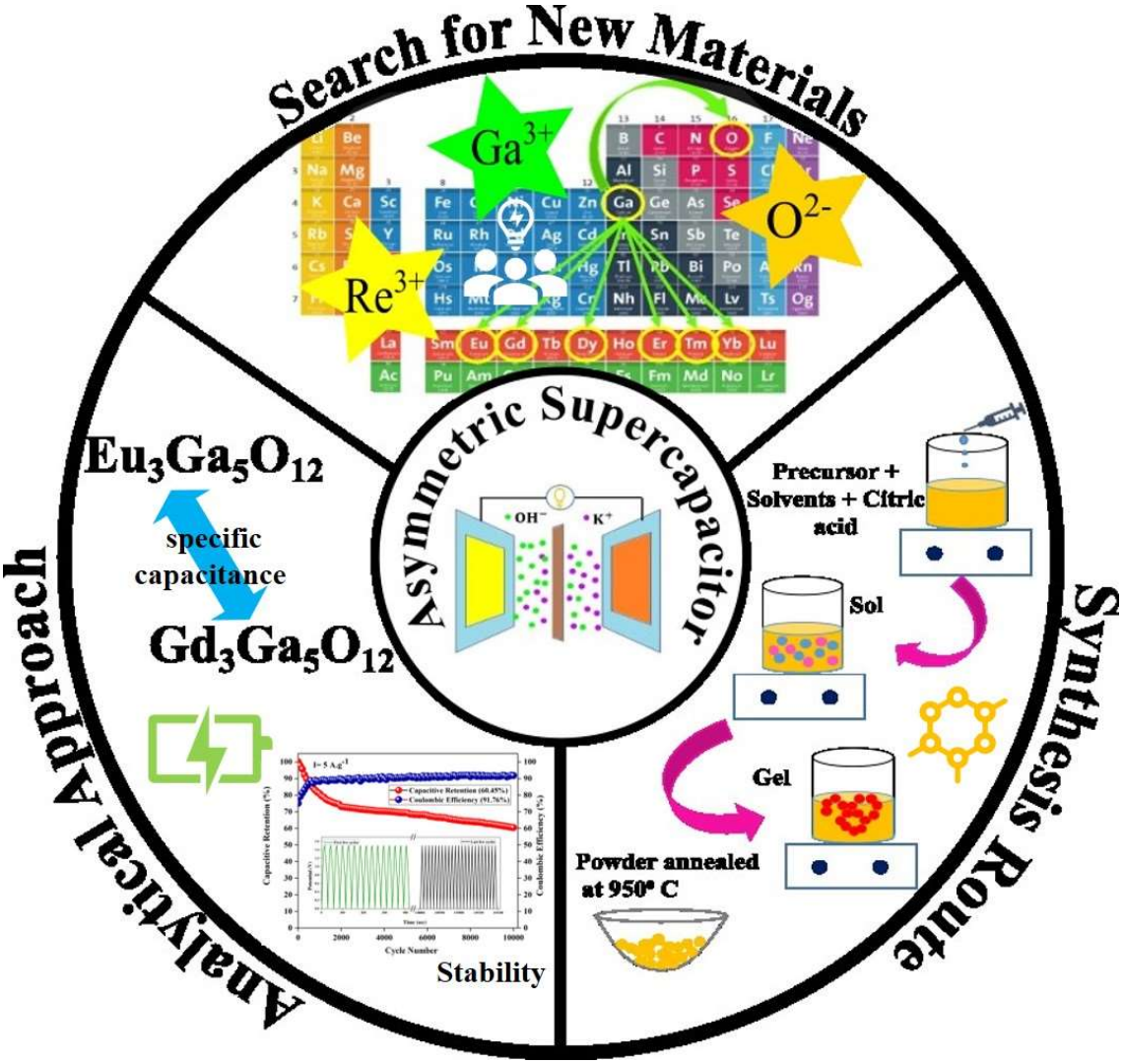

792

793

794

795 **Figure 1: Schematic illustration of search of best rare-earth gallium Garnets electrode**

796 **materials for asymmetric supercapacitor device fabrication**

797

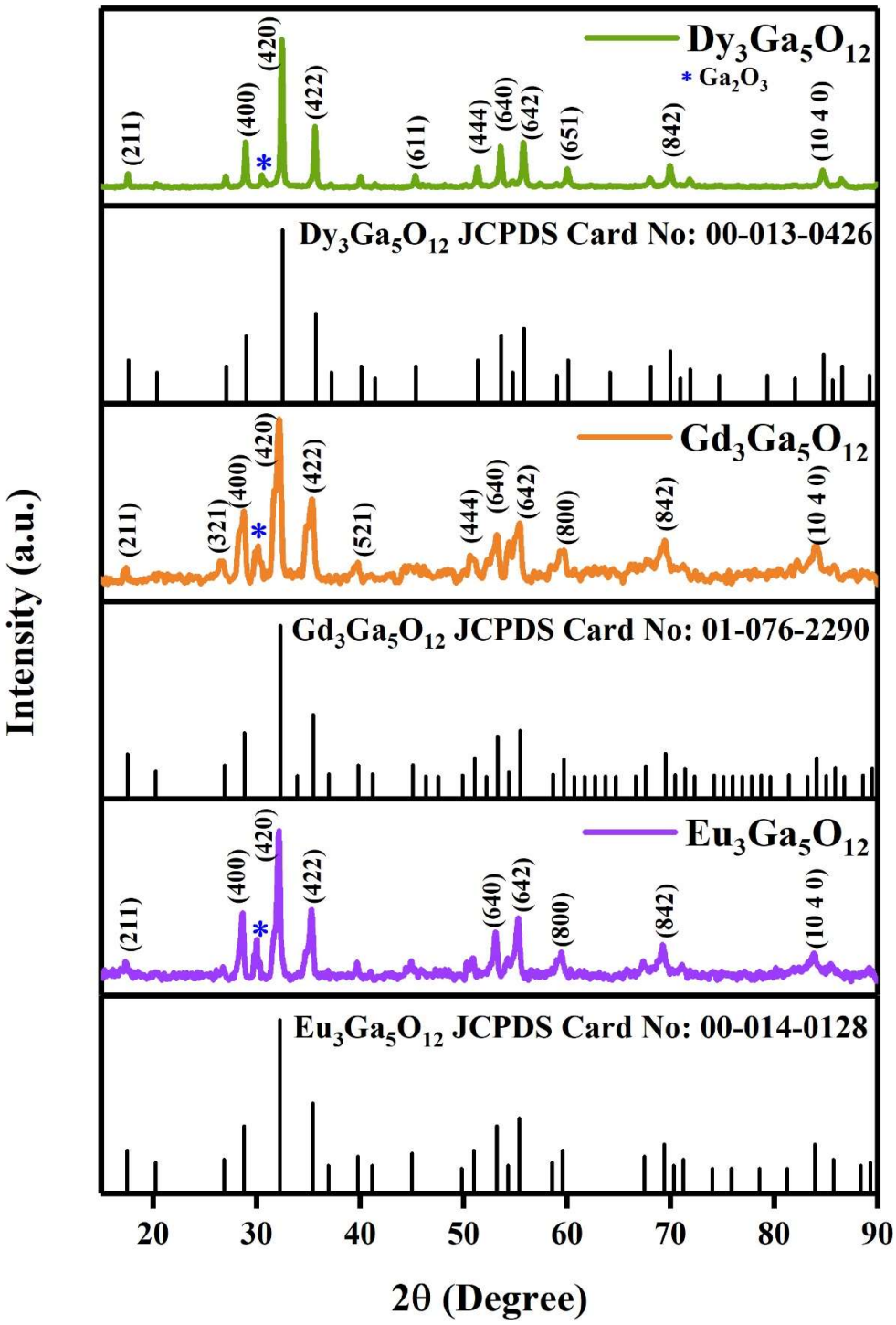

798

799 **Figure 2 (a): Comparative XRD pattern of $RE_3Ga_5O_{12}$ (RE = Eu, Gd and Dy)**

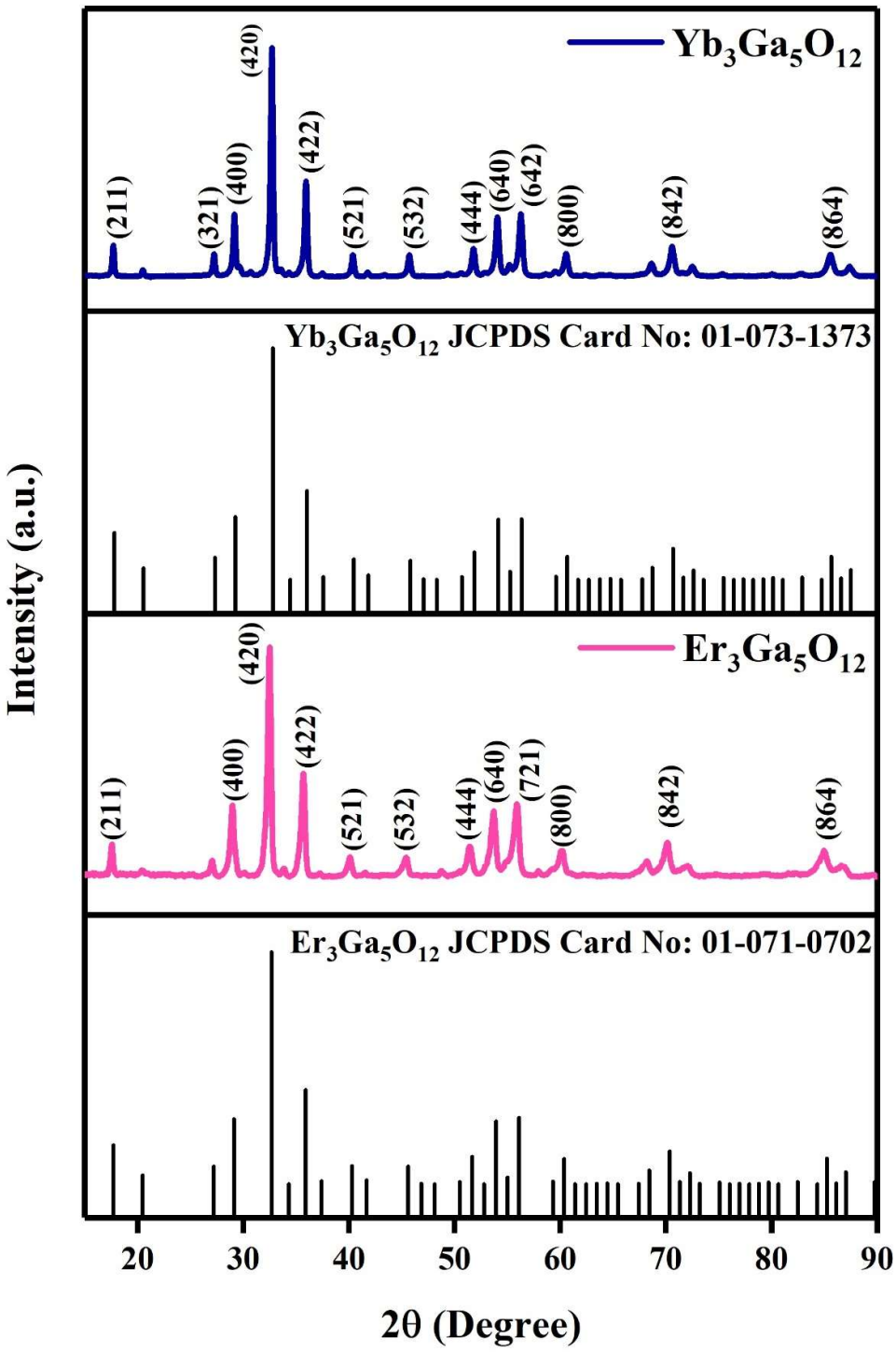

800

801 **Figure 2(b): Comparative XRD pattern of $RE_3Ga_5O_{12}$ (RE = Er and Yb)**

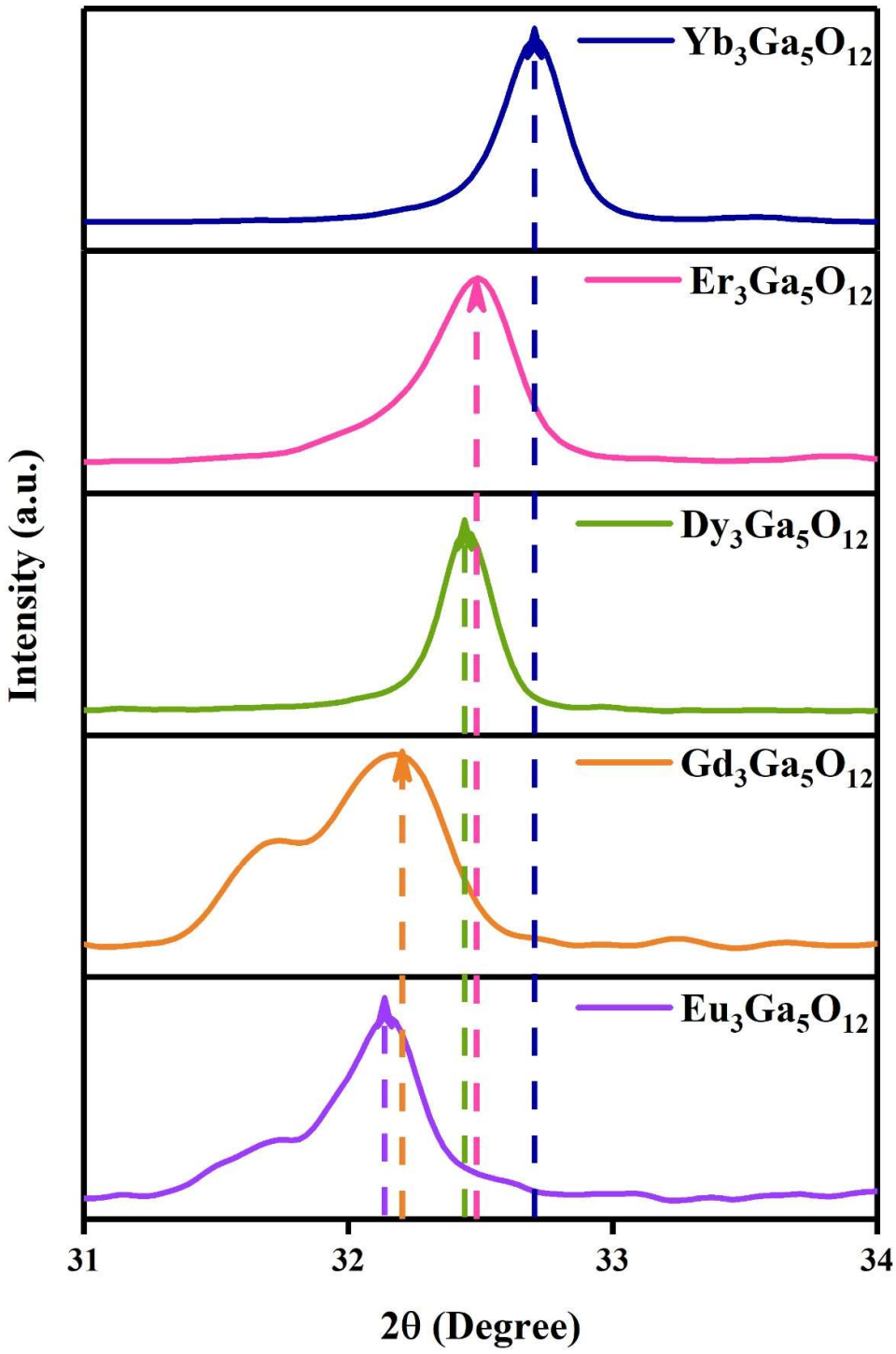

802

803 **Figure 3: Peak shift observed in the XRD reflections.**

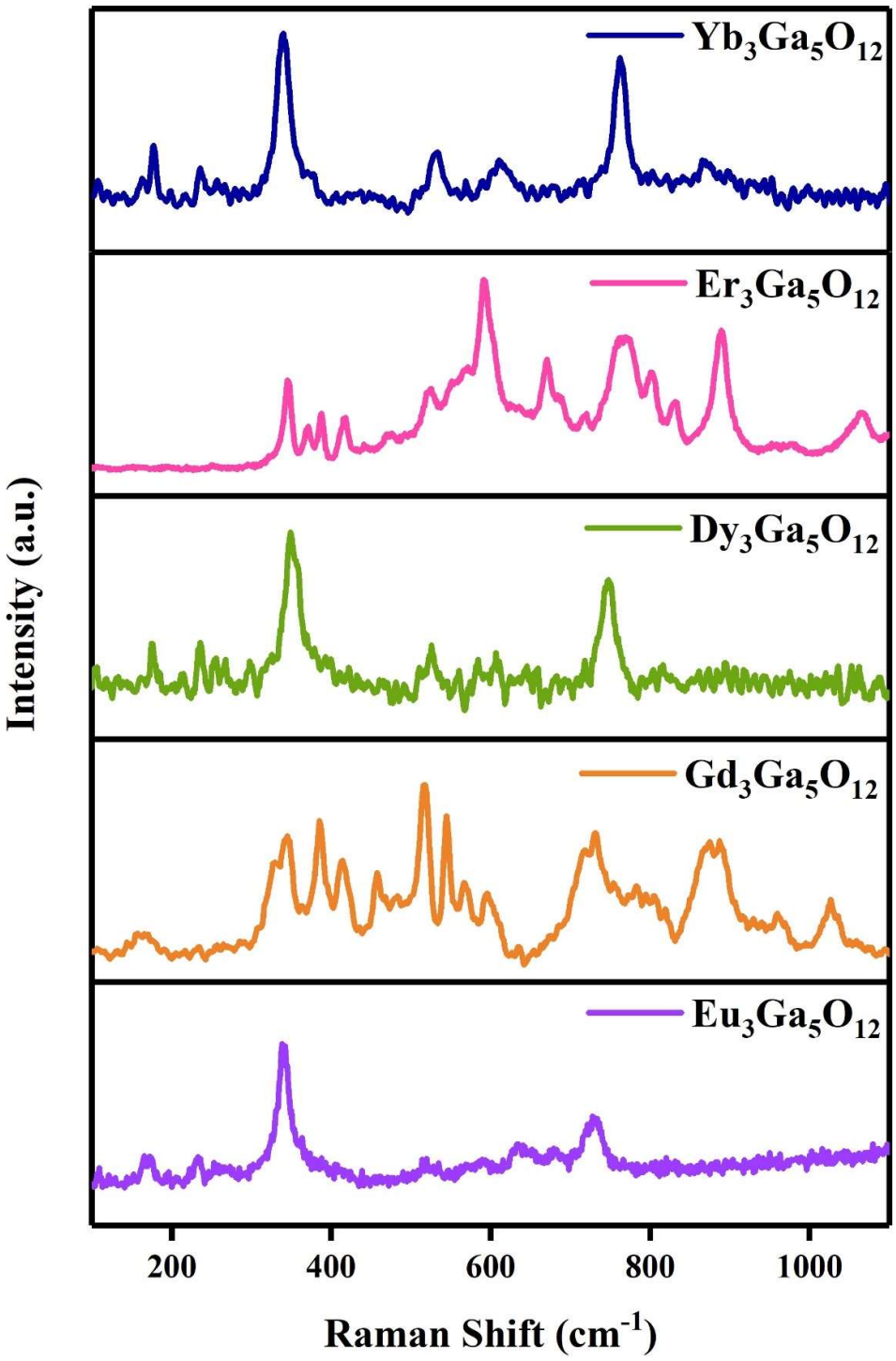

804

805 **Figure 4: Comparative Raman spectrum of $RE_3Ga_5O_{12}$ (RE = Eu, Gd, Dy, Er and Yb)**

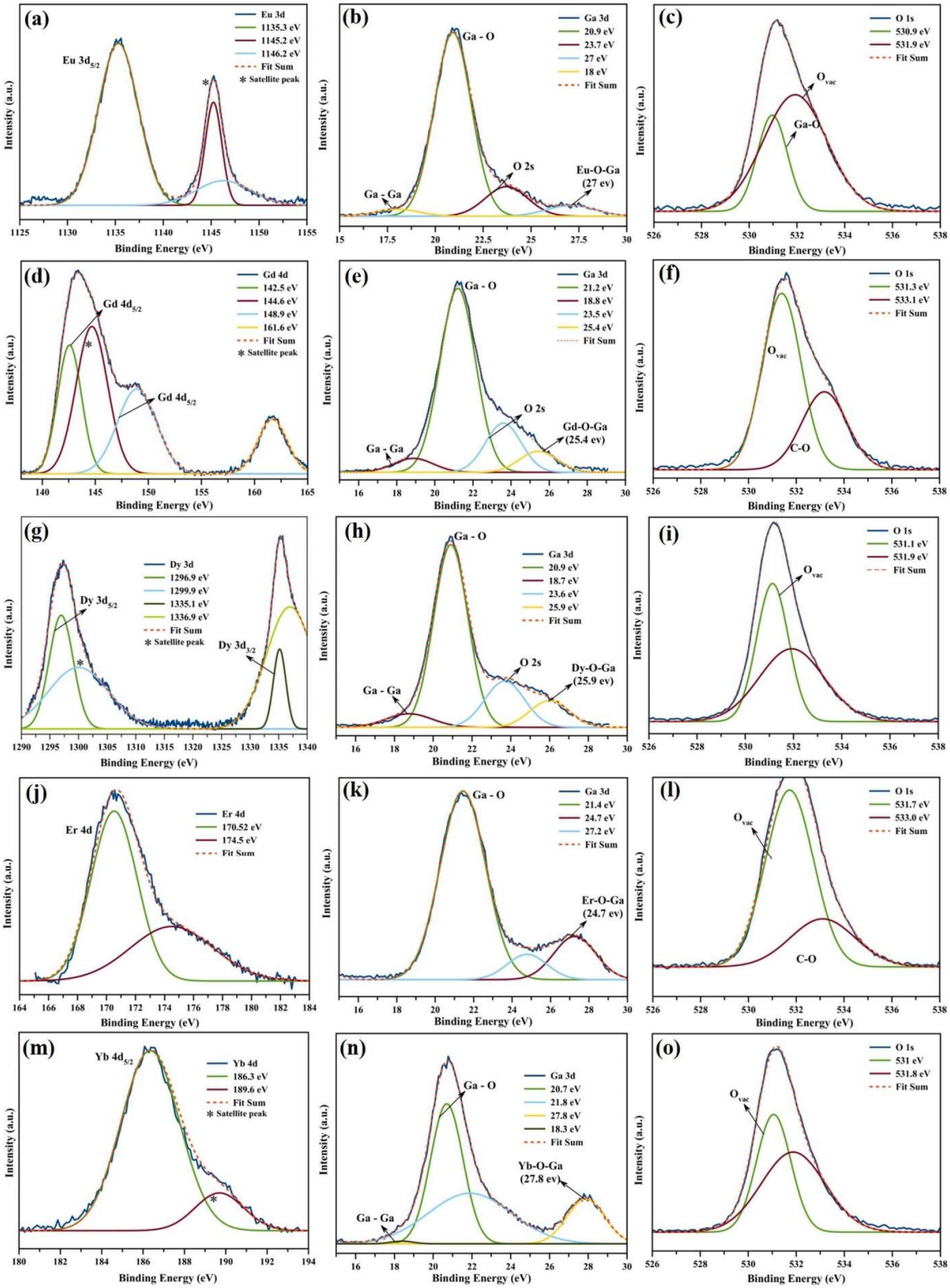

806

807 **Figure 5: XPS spectrum of $Eu_3Ga_5O_{12}$ (a-c), $Gd_3Ga_5O_{12}$ (d-f), $Dy_3Ga_5O_{12}$ (g-i),**

808 **$Er_3Ga_5O_{12}$ (j-l) and $Yb_3Ga_5O_{12}$ (m-o)**

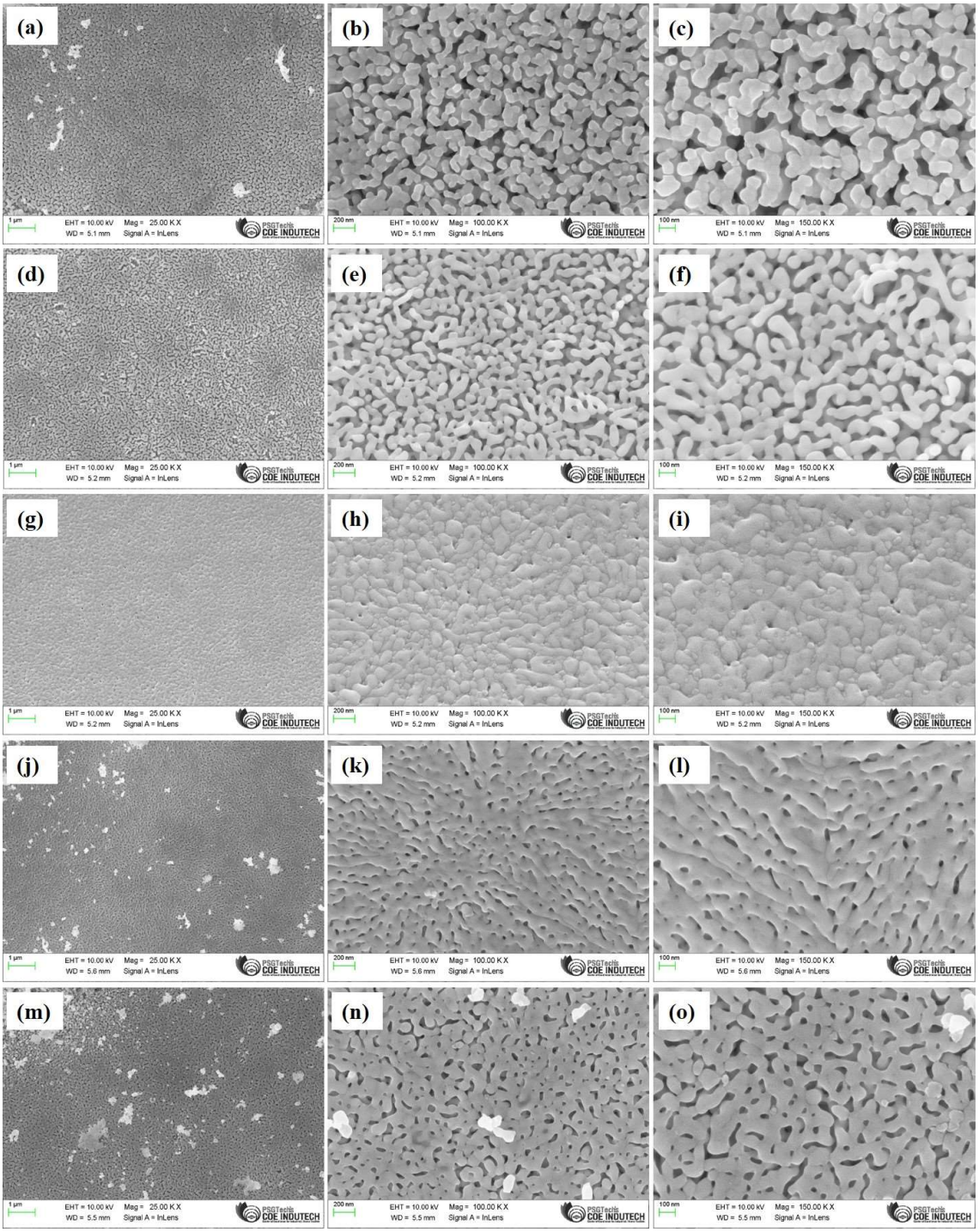

Figure 6: SEM micrographs of $Eu_3Ga_5O_{12}$ (a-c), $Gd_3Ga_5O_{12}$ (d-f), $Dy_3Ga_5O_{12}$ (g-i), $Er_3Ga_5O_{12}$ (j-l) and $Yb_3Ga_5O_{12}$ (m-o).

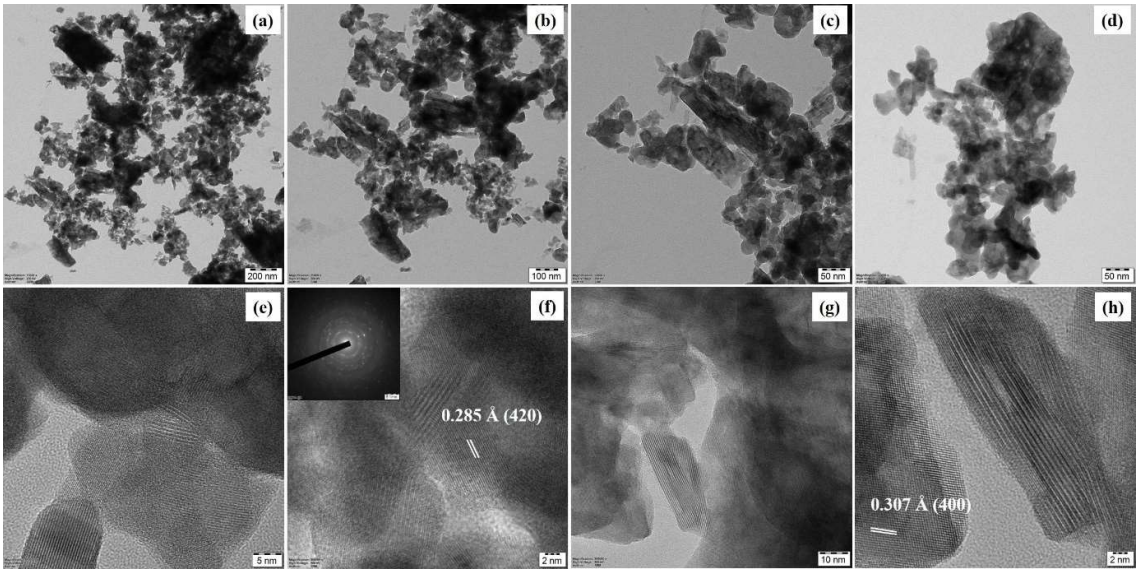

Figure 7: TEM and HRTEM images of $Eu_3Ga_5O_{12}$ (a-h).

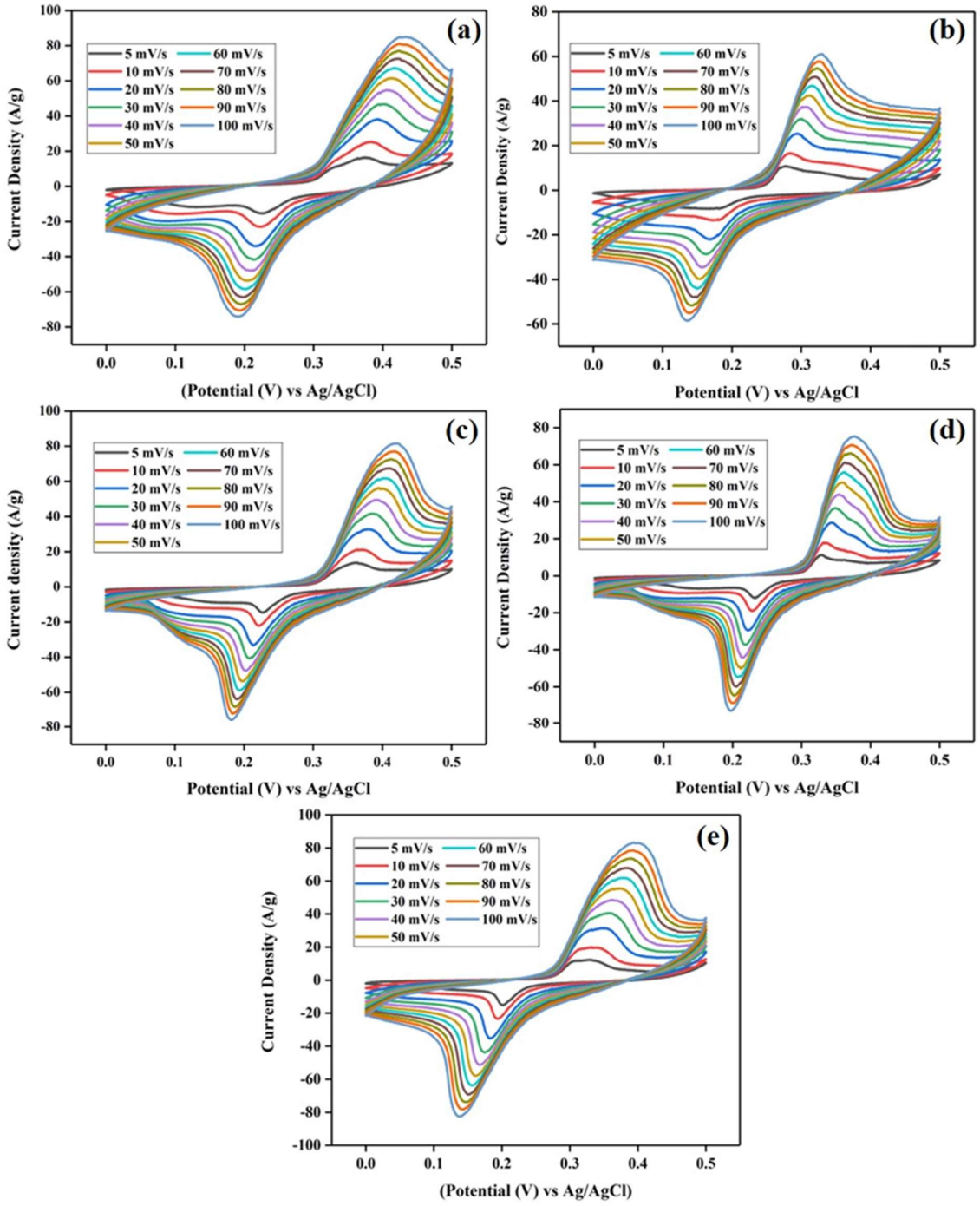

816

817

818 **Figure 8: CV voltammograms of $Eu_3Ga_5O_{12}$ (a), $Gd_3Ga_5O_{12}$ (b), $Dy_3Ga_5O_{12}$ (c),**

819 **$Er_3Ga_5O_{12}$ (d) and $Yb_3Ga_5O_{12}$ (e)**

820

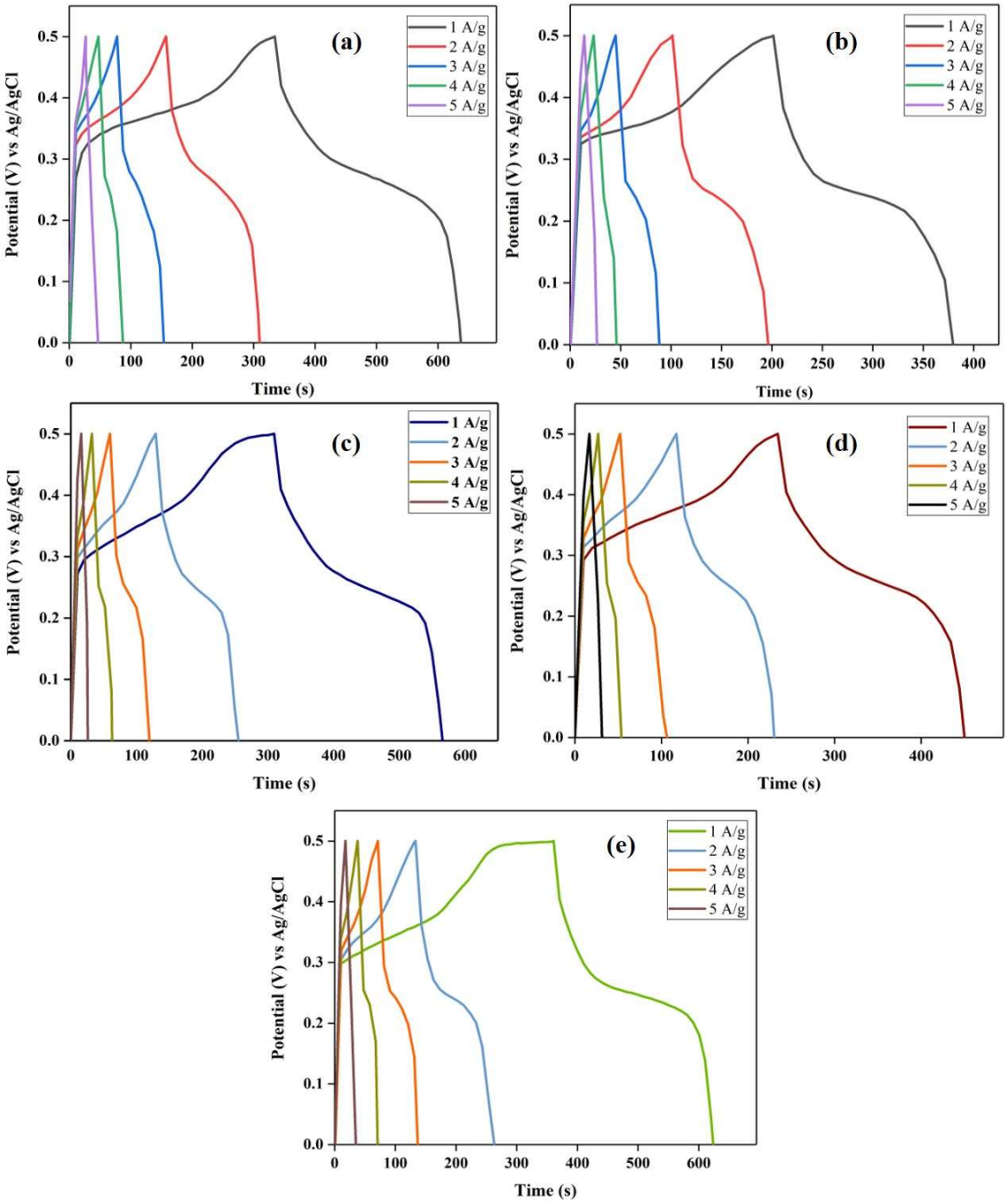

Figure 9: Comparative GCD curves of $Eu_3Ga_5O_{12}$(a), $Gd_3Ga_5O_{12}$(b), $Dy_3Ga_5O_{12}$(c), $Er_3Ga_5O_{12}$ (d) and $Yb_3Ga_5O_{12}$ (e)

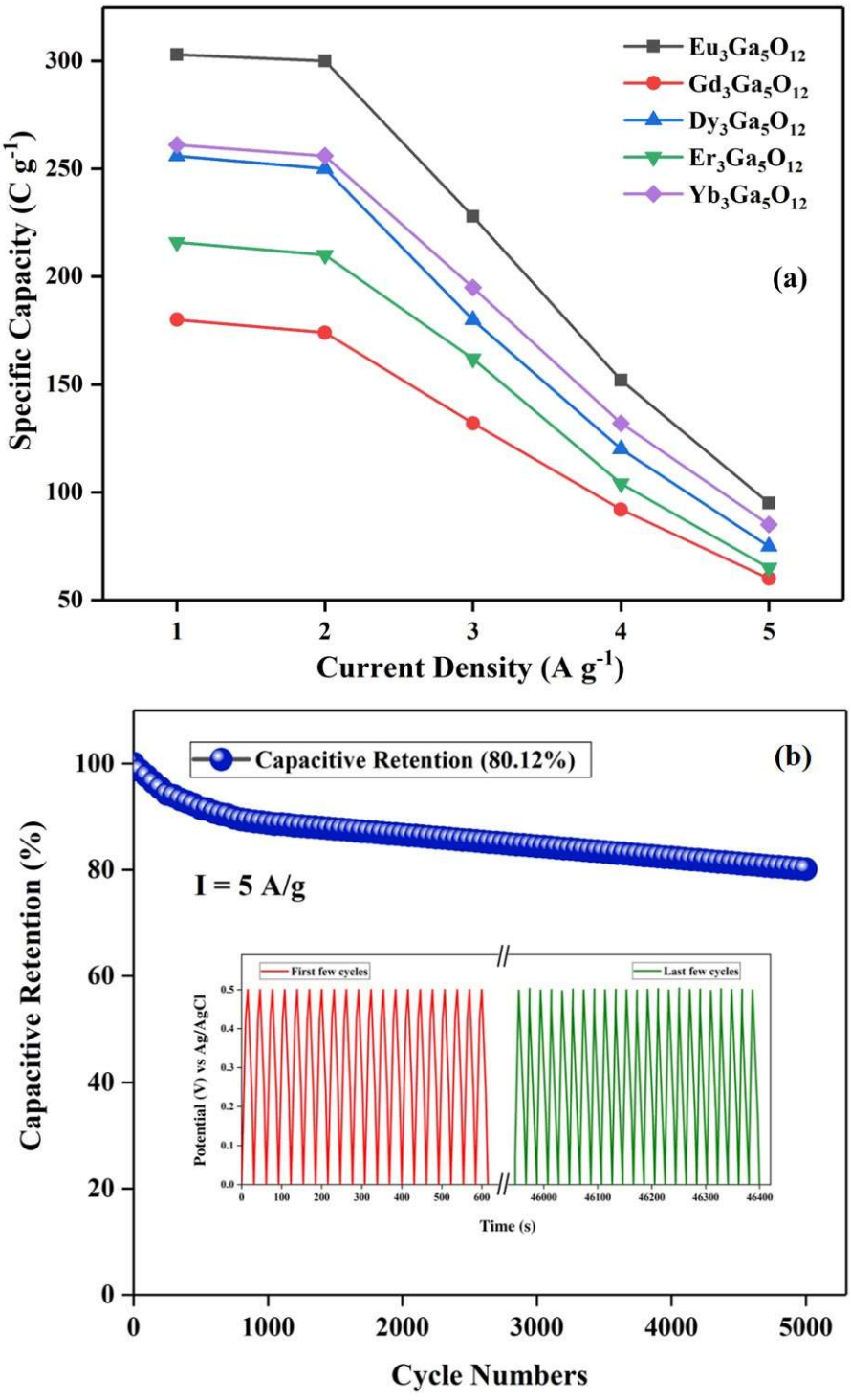

826

827 **Figure 10: (a) Specific capacity comparison of REGG (RE = Eu, Gd, Dy, Er and Yb)**

828 **and (b) stability graph of $Eu_3Ga_5O_{12}$ for 5000 cycles.**

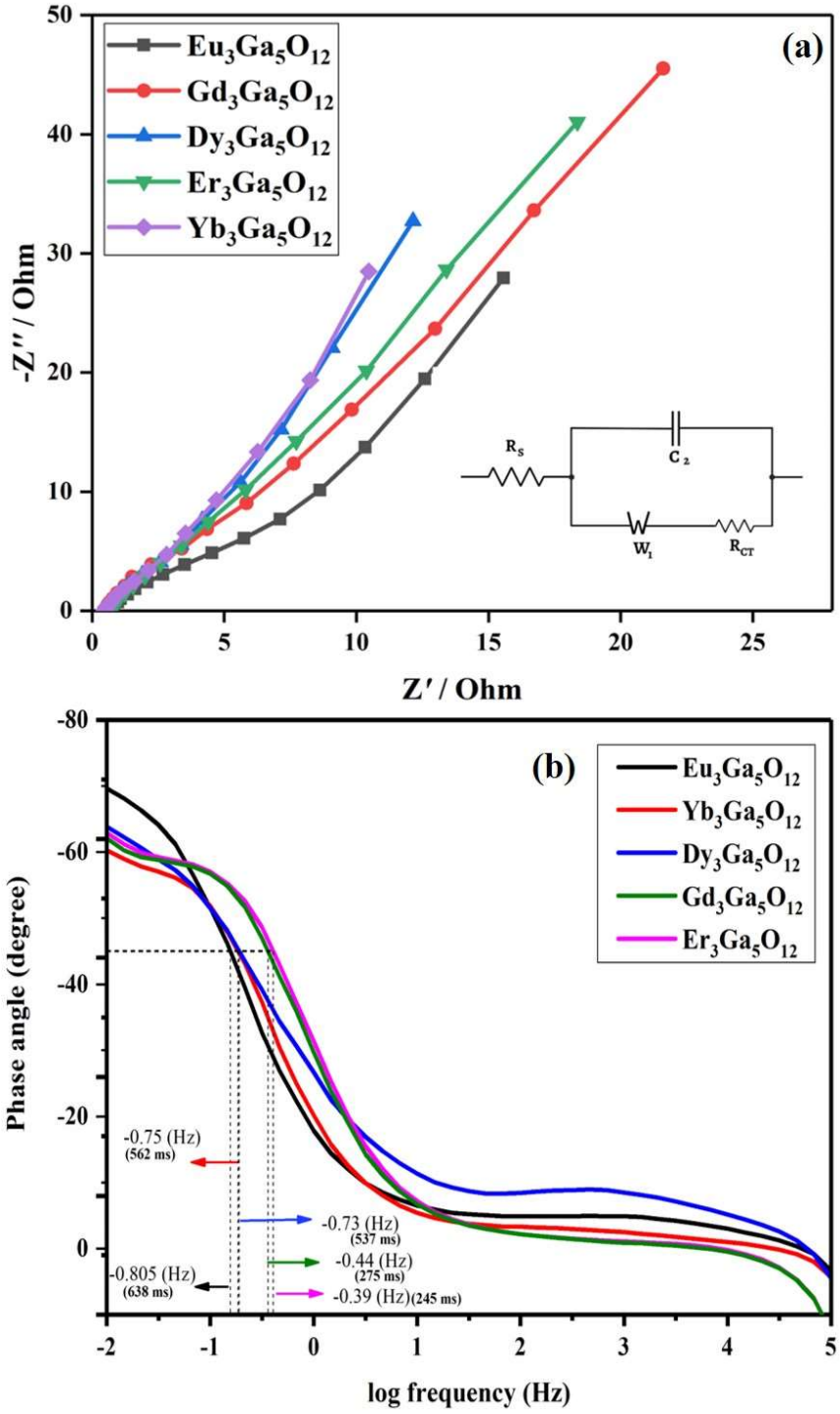

829

830

831 **Figure 11: Comparative EIS analysis (a) and Bode plot (b) of $RE_3Ga_5O_{12}$ (RE= Eu, Gd,**

832 **Dy, Er and Yb)**

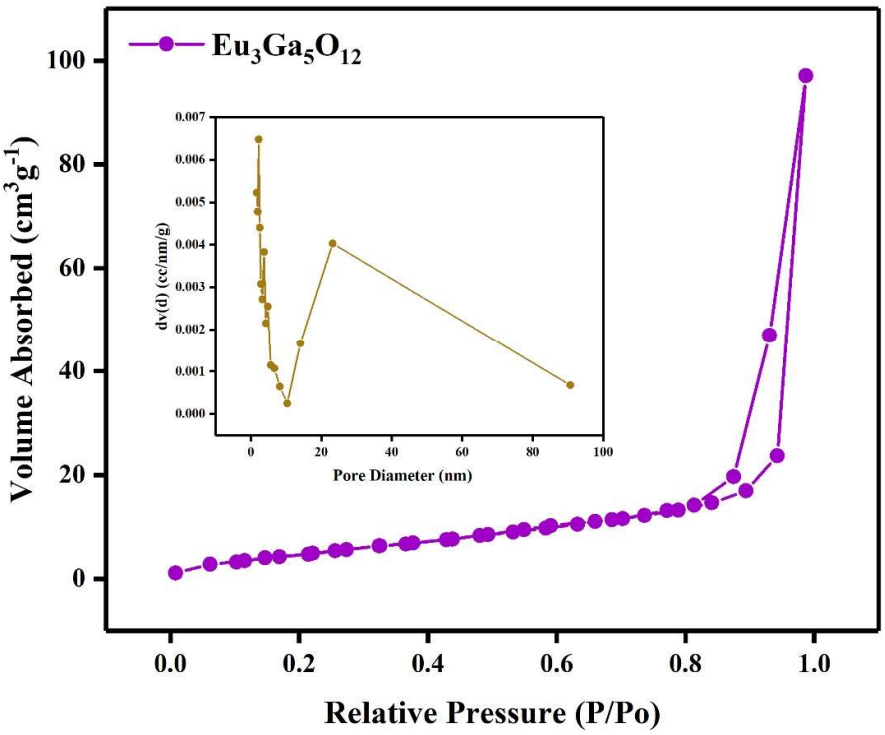

Figure 12: N_2 adsorption-desorption and BJH pore size distribution (inset) curves of $Eu_3Ga_5O_{12}$.

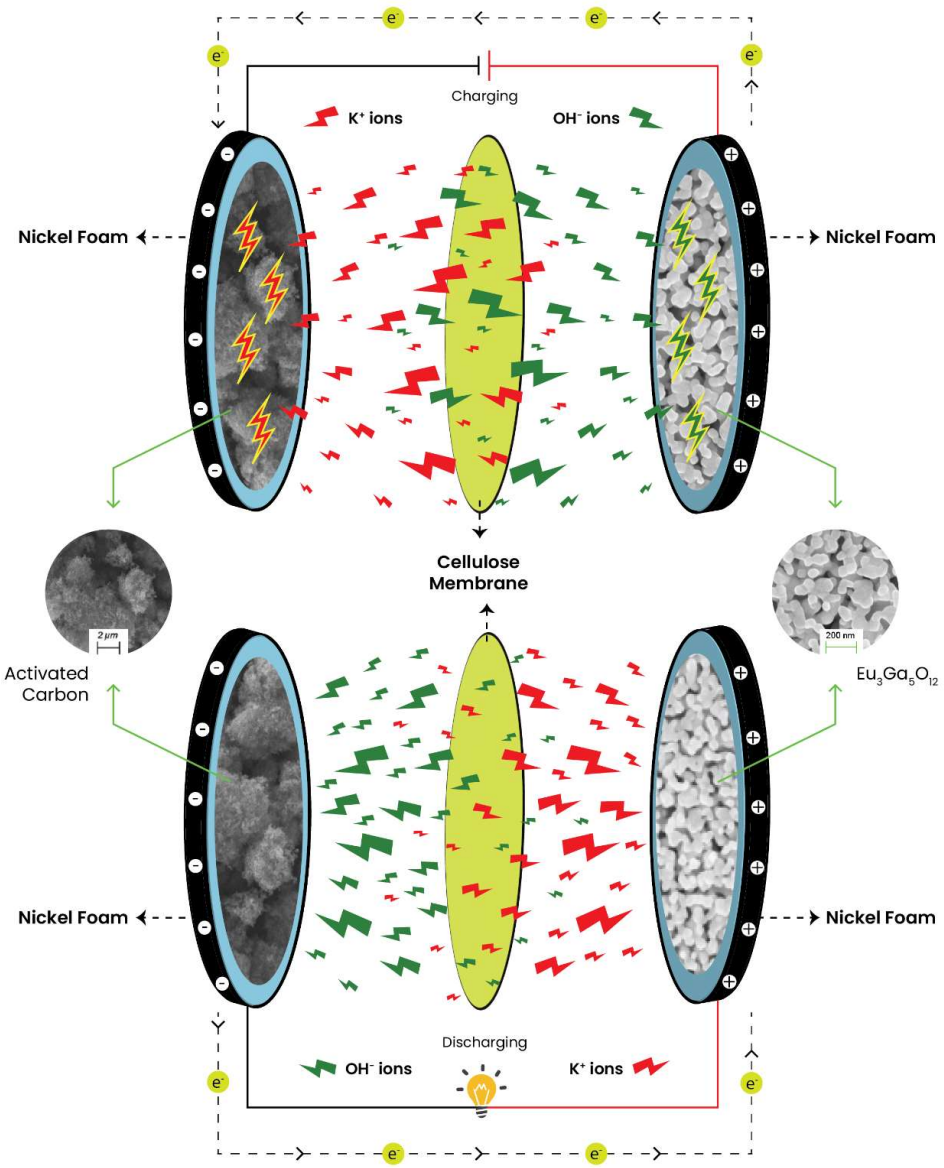

843

844 **Figure 13: Charge storage mechanism of fabricated $Eu_3Ga_5O_{12}$ based asymmetric**

845 **supercapacitor device.**

846

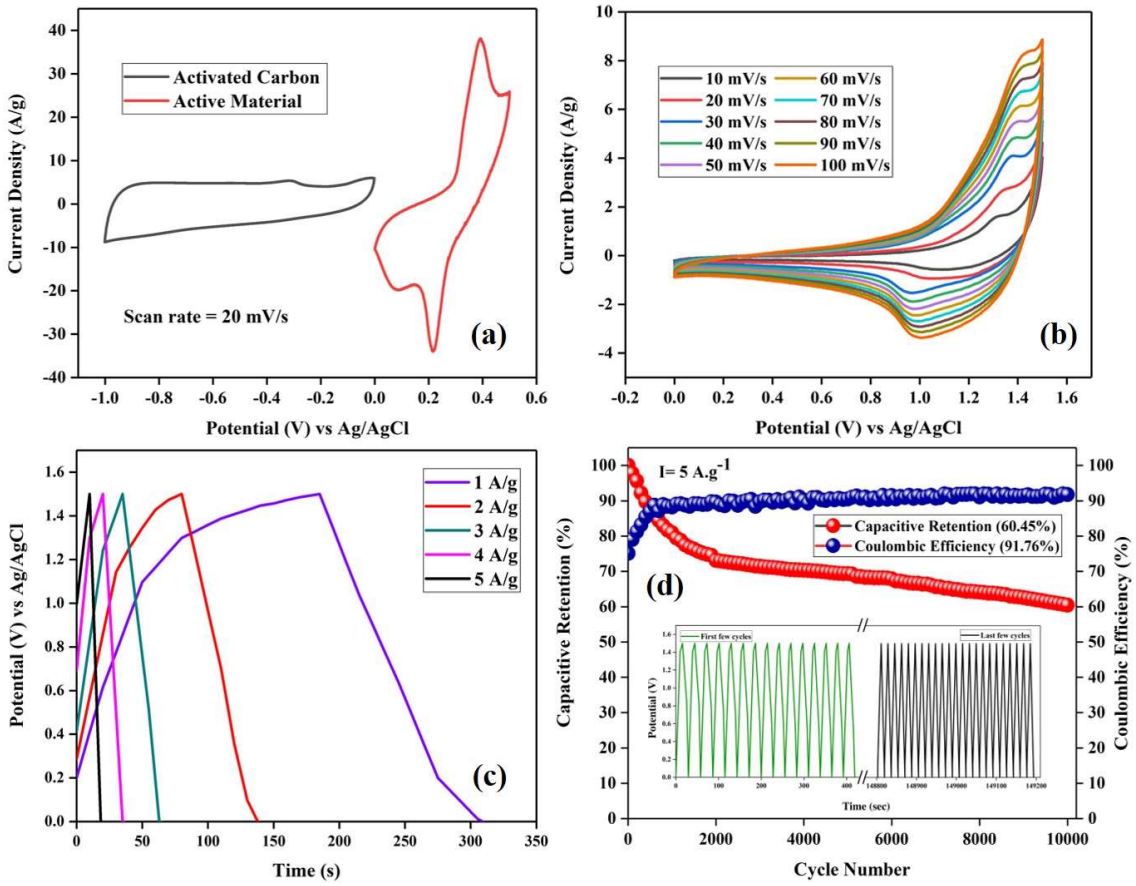

847

848

849 **Figure 14: (a) Comparative CV graph of activated carbon and active material**

850 **($Eu_3Ga_5O_{12}$) at a scan rate of 20 mV/s, (b) CV profile, (C) GCD graph and (d) Stability**

851 **curve of $Eu_3Ga_5O_{12}$ based asymmetric device.**

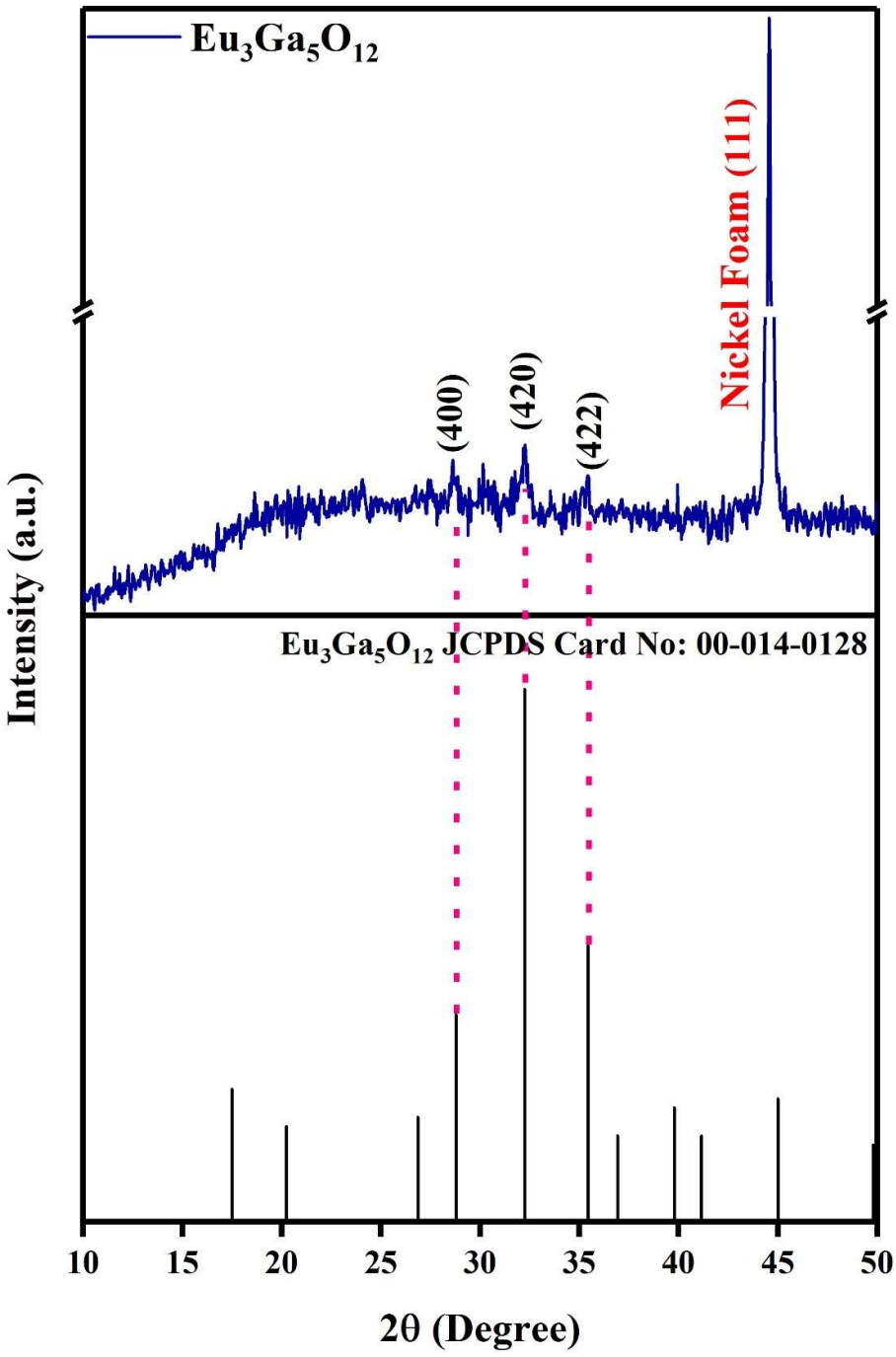

852

853 **Figure 15: XRD pattern of $Eu_3Ga_5O_{12}$ after stability analysis.**

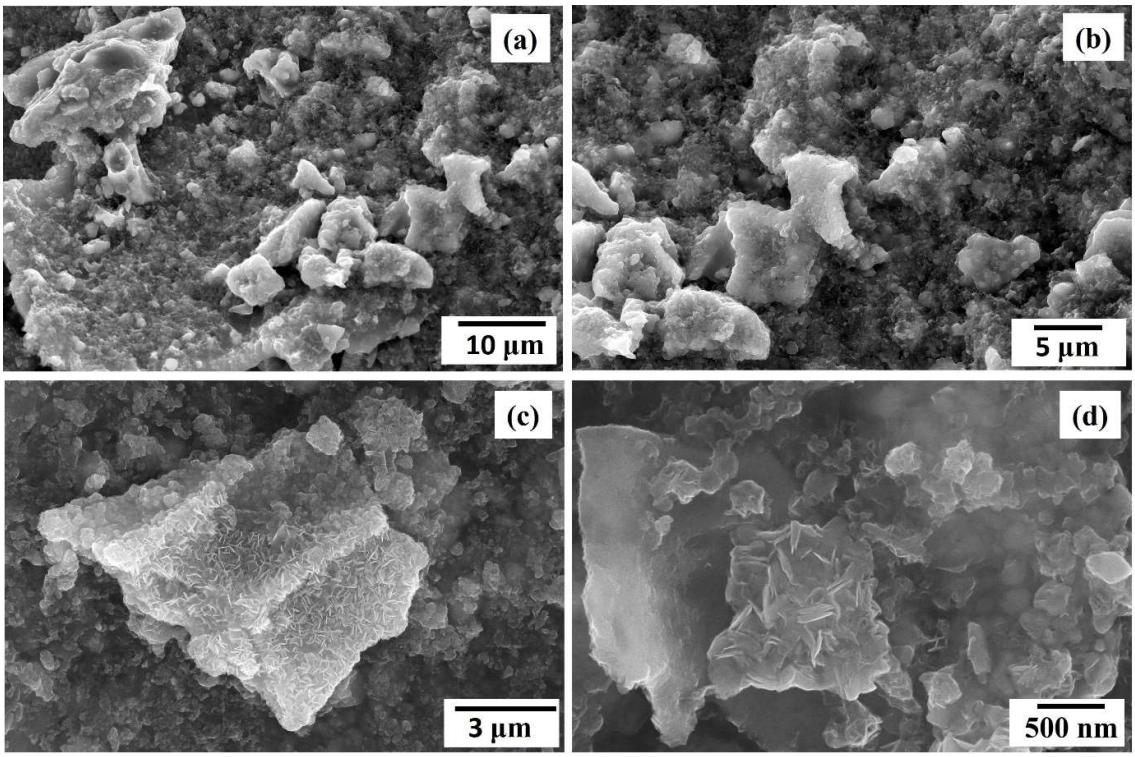

Figure 16: SEM micrographs of $Eu_3Ga_5O_{12}$ after 10,000 charge-discharge cycles.

Table 1: Comparison of specific capacity of REGG calculated from GCD analysis.

Rare Earth Gallium garnets	Specific capacity (C g^{-1}) at different current density (A g^{-1})				
	1 A g^{-1}	2 A g^{-1}	3 A g^{-1}	4 A g^{-1}	5 A g^{-1}
$Eu_3Ga_5O_{12}$	303	300	228	152	95
$Gd_3Ga_5O_{12}$	180	174	132	92	60
$Dy_3Ga_5O_{12}$	256	250	180	120	75
$Er_3Ga_5O_{12}$	216	210	162	104	65
$Yb_3Ga_5O_{12}$	261	256	195	132	85

877 **Table 2: Electrochemical performance comparison of $RE_3Ga_5O_{12}$ with literatures.**

878

Electrode Material	Synthesis Route	Electrolyte	Specific Capacity	Capacitive Retention	Reference
$GdCrO_3$	Solid State reaction	2 M KOH	227 C g^{-1} @ 0.5 mV/s	85% after 10000 cycles @ 1.5 A g^{-1}	[80]
$LaNiO_3$	Coprecipitation	3 M KOH	199 C g^{-1} @ 1 A g^{-1}	--	[81]
$MnCo_3/Mn_3O_4$	Hydrothermal	--	229.2 C g^{-1} @ 1 A g^{-1}	97.08% after 3000 cycles @ 1.5 A g^{-1}	[82]
Co_3O_4@Mo-Co_3O_4	Hydrothermal	2 M KOH	814 Cg^{-1}@1 A g^{-1}	90% after 4000 cycles	[83]
Sm_3GaO_6	Gel matrix	3 M KOH	374 Cg^{-1}@1 A g^{-1}	82.65 % after 5000 cycles	[84]
$Eu_3Ga_5O_{12}$	Gel matrix	3 M KOH	303 Cg^{-1}@ 1 A g^{-1}	80.12% over 5000 cycles	This work

879

880

881

882

883

884

885

886

887 **Table 3: Performance of Asymmetric device fabricated using $Eu_3Ga_5O_{12}$**

888

Potential Window (V)	Current Density ($A\ g^{-1}$)	Discharging Time (s)	Specific Capacity ($C\ g^{-1}$)	Energy Density ($Wh\ Kg^{-1}$)	Power Density ($W\ Kg^{-1}$)
1.5	1	125	125	39.06	1125
	2	58	116	36.25	2250
	3	29	87	27.18	3375
	4	15	60	18.75	4500
	5	8	40	12.5	5625

889

890

891

892

893

894

895

896

897

898

899

900 **Table 4: Comparison of fabricated $Eu_3Ga_5O_{12}$ based asymmetric supercapacitor device**

901 **with previous reports**

902

Electrode Material	Synthesis Route	Energy Density	Power Density	Capacitive retention	Reference
Tb and Y doped SnO_2@CuS	Hydrothermal	16.2 Wh Kg^{-1}	740 W Kg^{-1}	80.9% after 5000 cycles	[85]
Dy added spinel $ZnSm_2O_4$	Hydrothermal	1.85 Wh Kg^{-1}	--	95% after 2000 cycles	[86]
Gd_2NiMnO_6	Wet chemical route	20.23 Wh Kg^{-1}	421.75 W Kg^{-1}	--	[87]
Ga doped ZnO	Composite hydroxide mediated approach	10.8 Wh Kg^{-1}	200 W Kg^{-1}	80% after 3000 cycles	[88]
Sm_3GaO_6	Gel matrix	11.72 Wh Kg^{-1}	312.5 W Kg^{-1}	67.46% after 5000 cycles @ 5Ag^{-1}	[84]
$Eu_3Ga_5O_{12}$	Gel matrix	39.06 Wh Kg^{-1}	1125 W Kg^{-1}	60.45 % after 10000 cycles @5Ag^{-1}	This work

903